

## JGR Earth Surface

## RESEARCH ARTICLE

10.1029/2019JF005220

## Modeling Deltaic Lobe-Building Cycles and Channel Avulsions for the Yellow River Delta, China

## Key Points:

- Patterns of Yellow River deltaic lobe development are reproduced by a quasi-2-D numerical model
- Avulsions are less frequent and occur farther upstream when a delta lobe progrades
- The Yellow River deltaic system aggrades to 30% to 50% of bankfull flow depth before avulsion

## Supporting Information:

- Supporting Information S1

## Correspondence to:

A. J. Moodie,  
amoodie@rice.edu








## Citation:

Moodie, A. J., Nittrouer, J. A., Ma, H., Carlson, B. N., Chadwick, A. J., Lamb, M. P., & Parker, G. (2019). Modeling deltaic lobe-building cycles and channel avulsions for the Yellow River delta, China. *Journal of Geophysical Research: Earth Surface*, 124. <https://doi.org/10.1029/2019JF005220>

Received 21 JUN 2019

Accepted 20 SEP 2019

Accepted article online 15 OCT 2019

Andrew J. Moodie<sup>1</sup> , Jeffrey A. Nittrouer<sup>1</sup> , Hongbo Ma<sup>1</sup> , Brandee N. Carlson<sup>1</sup> , Austin J. Chadwick<sup>2</sup> , Michael P. Lamb<sup>2</sup> , and Gary Parker<sup>3,4</sup> 

<sup>1</sup>Department of Earth, Environmental and Planetary Sciences, Rice University, Houston, TX, USA, <sup>2</sup>Division of Geological and Planetary Sciences, California Institute of Technology, Pasadena, CA, USA, <sup>3</sup>Department of Civil and Environmental Engineering, University of Illinois at Urbana-Champaign, Champaign, IL, USA, <sup>4</sup>Department of Geology, University of Illinois at Urbana-Champaign, Champaign, IL, USA

**Abstract** River deltas grow by repeating cycles of lobe development punctuated by channel avulsions, so that over time, lobes amalgamate to produce a composite landform. Existing models have shown that backwater hydrodynamics are important in avulsion dynamics, but the effect of lobe progradation on avulsion frequency and location has yet to be explored. Herein, a quasi-2-D numerical model incorporating channel avulsion and lobe development cycles is developed. The model is validated by the well-constrained case of a prograding lobe on the Yellow River delta, China. It is determined that with lobe progradation, avulsion frequency decreases, and avulsion length increases, relative to conditions where a delta lobe does not prograde. Lobe progradation lowers the channel bed gradient, which results in channel aggradation over the delta topset that is focused farther upstream, shifting the avulsion location upstream. Furthermore, the frequency and location of channel avulsions are sensitive to the threshold in channel bed superelevation that triggers an avulsion. For example, avulsions occur less frequently with a larger superelevation threshold, resulting in greater lobe progradation and avulsions that occur farther upstream. When the delta lobe length prior to avulsion is a moderate fraction of the backwater length ( $0.3\text{--}0.5\bar{L}_b$ ), the interplay between variable water discharge and lobe progradation together set the avulsion location, and a model capturing both processes is necessary to predict avulsion timing and location. While this study is validated by data from the Yellow River delta, the numerical framework is rooted in physical relationships and can therefore be extended to other deltaic systems.

## 1. Introduction

The development of a fluvial-deltaic system over timescales of decades to millenia is characterized by repeated lobe switching: a process whereby a primary distributary channel progrades basinward, building a lobe until an avulsion causes the distributary channel to shift, generating a new lobe (Frazier, 1967). Over time, lobes amalgamate and produce a delta that typically maintains an approximately radially symmetric planform (Figure 1). Many large, lowland fluvial-deltaic systems require tens to thousands of years between avulsions (Jerolmack & Mohrig, 2007). As a result, field studies of modern channel avulsions have identified, at most, only a few events (Assine, 2005; Brizga & Finlayson, 1990; Coleman, 1988; Donselaar et al., 2013; Frazier, 1967; Jerolmack, 2009; Jones & Harper, 1998; McCarthy et al., 1992; Richards et al., 1993; Smith et al., 1989; Törnqvist, 1994; Wells & Dorr, 1987; Xue, 1993; van Gelder et al., 1994). Insights into deltaic lobe building have benefited from outcrop and experimental research, where multiple avulsions can be examined (e.g., Hajek & Wolinsky, 2012; Mohrig et al., 2000). However, outcrop studies of avulsions are subject to uncertainty around reconstructing relevant system characteristics, including river slope, regional geography, and the timing of events (Lynds et al., 2014; Sheets et al., 2002). Experimental studies document delta growth through many lobe-building cycles and are valuable because system boundary conditions are controlled (Hoyal & Sheets, 2009; Kim et al., 2006; Kim & Jerolmack, 2008; Paola et al., 2009; Whipple et al., 1998; Sheets et al., 2002; Reitz & Jerolmack, 2012; Ganti et al., 2016b; Ganti et al., 2016a). Additionally, physically based numerical models provide the opportunity to assess system responses to changing boundary conditions over a range of spatiotemporal scales (Chadwick et al., 2019; Kim et al., 2009; Moran et al., 2017; Parker, Paola, Whipple, & Mohrig, 1998; Parker, Paola, Whipple, Mohrig, Toro-Escobar, et al., 1998; Paola, 2000; Parker et al., 2008a, 2008b; Ratliff et al., 2018; Sun et al., 2002).

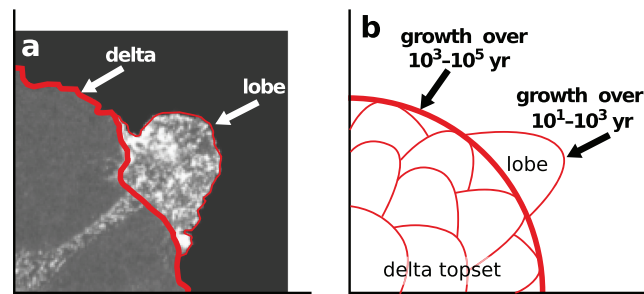


**Figure 1.** (a) Delta system edge (thick red line) and lobe extent (thin red line), traced from a photograph of a fan from a physical experiment (Reitz & Jerolmack, 2012). (b) Sketch demonstrating a conceptual model for deltaic system growth, where deltas grow through a series of lobe-building cycles, with typical timescales of development indicated (Jerolmack & Mohrig, 2007).

The ability to predict when and where a natural lobe-switching avulsion will occur is a major motivator for fluvial-deltaic research, because the unanticipated civil disruption associated with flooding and channel relocation is at odds with society's desire for landscape stability and continued socioeconomic use of deltaic landforms and channels. Additionally, on highly anthropic deltas, river engineering such as upstream dams and flow diversions restricts flow pathways and collectively alters sediment delivery necessary to sustain deltas and coastlines (Nittrouer & Viparelli, 2014). Avulsion is thus a double-edged sword: Engineering limits avulsion hazards but also diminishes sediment supply and enhances land loss; yet allowing avulsions to occur naturally threatens the economic utility of deltas by causing the rapid displacement of the channel and land flooding. To both minimize the impact of flooding and ensure sediment delivery to the coast, engineered avulsions and diversions have been implemented to approximate natural delta development (Allison & Meselhe, 2010; Paola et al., 2011; Peyronnin et al., 2013; van Gelder et al., 1994; Xu, 2003; Yuill et al., 2016). Accurately assessing the spatiotemporal likelihood of natural avulsions could inform targeted engineering practices that seek to minimize flooding while maximizing sediment delivery to the coastline.

An important scaling metric in fluvial-deltaic systems is the extent of channel impacted by nonuniform flow, known as the backwater length  $\bar{L}_b$  (e.g., Paola & Mohrig, 1996):

$$\bar{L}_b = \frac{H_m}{S_0}, \quad (1)$$

where  $H_m$  is the flow depth at the channel outlet and  $S_0$  is the reach-averaged channel bed slope. Throughout this article, an overline is used to denote a value calculated by a scaling metric (e.g., equation (1)). In the backwater reach during low and moderate water discharge, a downstream deceleration of reach-average flow velocity results in a spatial divergence in sediment transport, and as a result, the channel bed aggrades (Nittrouer et al., 2012; Parker, 2004; Parker et al., 2008a, 2008b; Snyder et al., 2006). High water discharge events (i.e., floods) cause a downstream acceleration of flow velocity by hydrodynamic drawdown, which erodes the channel bed near the river mouth (Lamb et al., 2012). The net effect of the two conditions is to produce a preferred region of net bed aggradation (Chadwick et al., 2019; Chatanantavet & Lamb, 2014; Chatanantavet et al., 2012; Ganti et al., 2016a, 2016b), which raises river stage and, in time, superelevates the water surface above the floodplain. This produces a gravitational instability favoring an avulsion (Bryant et al., 1995; Edmonds et al., 2009; Mohrig et al., 2000; Slingerland & Smith, 2004; Smith et al., 1989). Indeed, numerous studies have demonstrated that the avulsion length ( $L_A$ )—the distance from contemporaneous coastline to avulsion location—scales with the backwater length ( $\bar{L}_b$ ; Chatanantavet et al., 2012; Ganti et al., 2014, 2016a, 2016b; Zheng et al., 2019; Jerolmack & Swenson, 2007).

The avulsion timescale ( $\bar{T}_A$ ) is inversely related to the rate of sediment aggradation on the channel bed  $v_a$ :

$$\bar{T}_A = \frac{\beta H_{bf}}{v_a}, \quad (2)$$

where  $H_{bf}$  is a characteristic channel bankfull flow depth and  $\beta$  is a coefficient that varies between 0.3 and 1 on modern delta systems but may be  $>1$  for fan-delta systems (Ashworth et al., 2004; Bryant et al., 1995; Ganti et al., 2014, 2016a, 2016b; Jain & Sinha, 2004; Jerolmack & Mohrig, 2007; Heller & Paola, 1996; Martin et al., 2009; Moran et al., 2017; Mohrig et al., 2000; Stouthamer & Berendsen, 2001; Törnqvist, 1994).

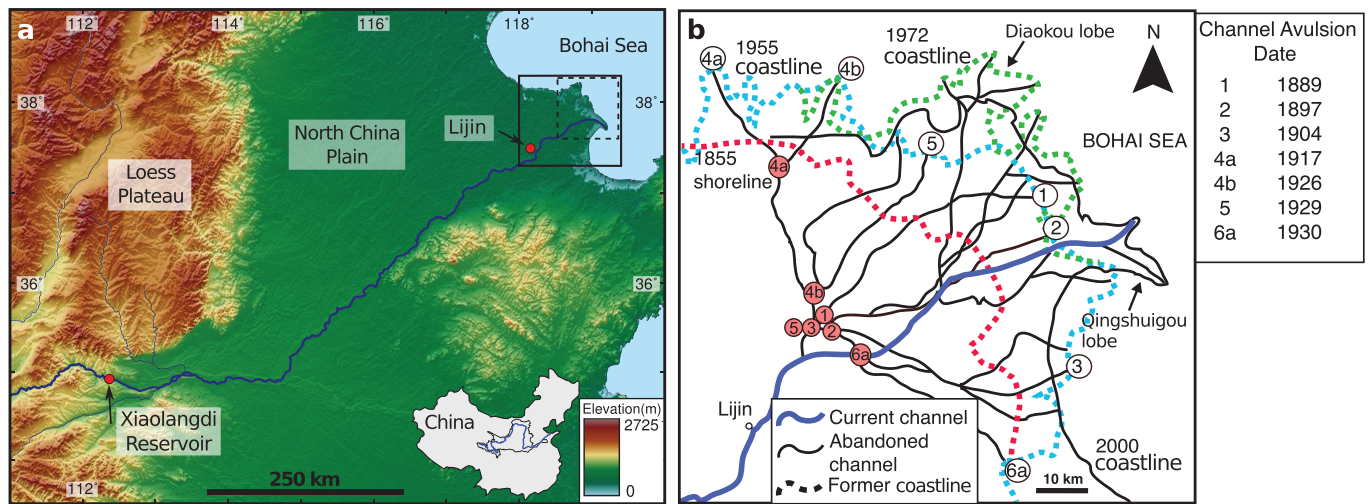


**Figure 2.** (a) Location map of the lower Yellow River, where it exits the Loess Plateau and traverses ~900 km to the Bohai Sea. Lijin is situated at approximately the modern delta apex. Solid line box shows the approximate extent of Figure 2b. Dashed line shows the approximate extent of Figure 4a. (b) Historical record of deltaic avulsions and coastline positions for the Yellow River delta, China (reproduced from Ganti et al., 2014, after Pang & Si, 1979; van Gelder et al., 1994).

The time to avulsion is minimized in the backwater region because channel bed aggradation is enhanced here (equation (2); Chatanantavet et al., 2012; Jerolmack, 2009; Jerolmack & Swenson, 2007; Hoyal & Sheets, 2009; Lamb et al., 2012; Nittrouer et al., 2012). An avulsion is also dependent on a “trigger” event, typically a flood, that produces a sustained levee breaching flow and initiates a new channel (Edmonds et al., 2009; Ganti et al., 2016b; Hajek & Wolinsky, 2012; Mohrig et al., 2000; Slingerland & Smith, 2004). Water flow through a crevasse can also reoccupy a relict channel pathway, which may be a preexisting low on the floodplain (Edmonds et al., 2009; Reitz & Jerolmack, 2012; Reitz et al., 2010; Slingerland & Smith, 2004).

Experimental and numerical studies indicate that subaqueous levee growth near the river outlet leads to channel extension (Chatanantavet & Lamb, 2014; Falcini et al., 2014; Mariotti et al., 2013; Rowland et al., 2009, 2010). While some previous modeling research has included delta progradation using a downstream moving boundary condition, most models do not simulate channelization and lobe progradation (Chatanantavet & Lamb, 2014; Chatanantavet et al., 2012; Parker, 2004; Parker et al., 2008b). Furthermore, as a delta with similar sized lobes migrates basinward, it is predicted that the avulsion node should migrate basinward as well, because the avulsion location is linked to the distance to the coastline (i.e., backwater length scaling; Jerolmack, 2009; Ganti et al., 2014). Basinward avulsion node migration is recognized in physical experiments (Ganti et al., 2016a, 2016b) but has been only minimally documented in numerical modeling (Chadwick et al., 2019). As such, the influence of delta lobe progradation on avulsion timing and location remains unclear.

Herein, a quasi-two-dimensional (2-D) numerical model is developed to explicitly account for multiple lobe progradation and avulsion cycles so as to mimic overall delta growth. The model is applied to the Yellow River delta (China) as a case study because this system is composed of lobes that scale with the estimated backwater length (Ganti et al., 2014; Yu, 2002) and because a comprehensive record of avulsions makes this system arguably the best lowland delta in the world to compare with numerical predictions. This study also serves to determine future avulsion location and timing for the Yellow River delta and thus guide decisions about engineered diversions.

## 2. Yellow River Fluvial-Deltaic System

The Yellow River drainage basin stretches across northern China, with water flowing primarily from west to east, draining an area of 752,000 km<sup>2</sup> over a river length of 5,460 km, before entering the Bohai Sea (Figure 2a; Ren & Walker, 1998; Saito et al., 2000; van Gelder et al., 1994). A portion of the basin includes the Loess Plateau, an unconsolidated sediment deposit hundreds of meters thick composed of very fine sand and silt (Ma et al., 2017; Saito et al., 2001; Yu, 2002; Zhu et al., 2018). This material is readily eroded and contributes to the sediment discharge, which exceeds 1 Gt/year (Yu, 2002). Sediment concentration in the

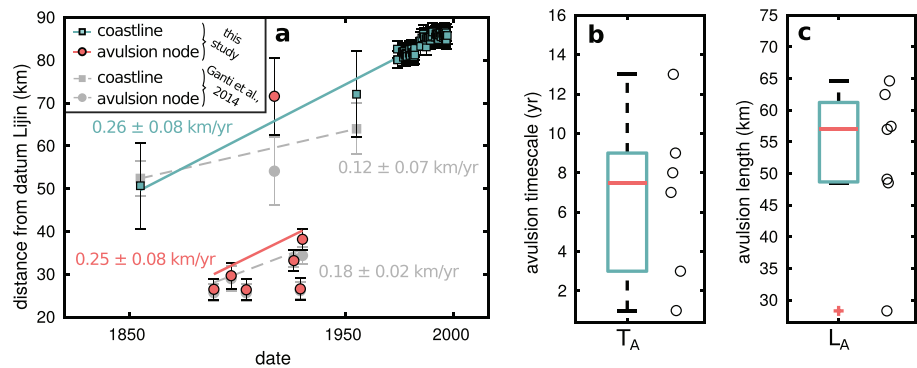


**Figure 3.** (a) Radially averaged coastline position (squares) measured as distance from Lijin and avulsion location (circles) measured as streamwise distance from Lijin show progradation of the deltaic coastline and forward stepping of deltaic avulsions through time; data extracted from the historical record and satellite imagery (Figures 2b and 4b). Discrepancy between this study and Ganti et al. (2014) is due to georeferencing uncertainty, addition of new data, and difference in regression methods (supporting information S1). (b) Boxplot of avulsion time (actual data shown to side,  $n = 6$ ),  $T_{A,YR} = 7 \pm 2$  year (Ganti et al., 2014). (c) Boxplot of avulsion length, as measured streamwise from the coastline to the avulsion location (actual data shown to side,  $n = 7$ ), mean =  $L_{A,YR} = 52.5 \pm 12.3$  km.

Yellow River is 1 to 2 orders of magnitude higher than other large lowland rivers (e.g., Mississippi River and Amazon River; Wang & Liang, 2000; Yu, 2002). As such, the delta is dynamic (e.g.,  $T_A = 10^1$  year estimated from equation (2), Jerolmack & Mohrig, 2007). For the lower 200 km of the Yellow River, flow depth is 2–6 m, and channel width is 300–500 m, with a mean value of approximately 400 m. In-channel sedimentation has driven frequent lobe-switching channel avulsions and progradation into the Bohai Sea (van Gelder et al., 1994; Wang & Liang, 2000).

Since 1855, when the Yellow River avulsed to the north of the Shandong Peninsula, multiple lobes have amalgamated to build a delta into the Bohai Sea, totaling an area approximately 6,000 km<sup>2</sup> (Figures 2a and 2b; Fan et al., 2006; Pang & Si, 1979; van Gelder et al., 1994; Xue, 1993; Yu, 2002). The natural avulsion timescale of the Yellow River delta prior to major engineering is  $T_{A,YR} = 7 \pm 2$  year (Ganti et al., 2014; Figure 3). The streamwise distance from the location of avulsions to the contemporaneous coastline for the period from 1889 to 1931 yields the avulsion length mean and standard deviation  $L_{A,YR} = 52.5 \pm 12.3$  km, which is consistent with the estimated backwater range of  $\bar{L}_b = 21$ –54 km (Ganti et al., 2014). The avulsion location has stepped basinward over time at a rate of 0.18–0.25 km/year (Figures 2b and 3a; Ganti et al., 2014). However, a decreasing trend in water discharge and ongoing river engineering in the past century has also contributed to downstream shifting of the avulsion location (Ganti et al., 2014; Kong et al., 2015; Liu et al., 2012; Wang et al., 2006; Wang et al., 2007). Discrepancy between data shown in this study and that of Ganti et al., 2014 (2014; Figure 3a) is due to georeferencing uncertainty, additional new data produced herein, and different regression approaches (supporting information S1).

In 1976, the channel course of the Yellow River was changed through an engineered avulsion, which redirected the channel from the northern Diaokou course to the eastern Qingshuigou course (Figure 4a). The Qingshuigou pathway was maintained until 1996, when the lower ~20 km of the course was again diverted (Yu, 2002). Thus, the Qingshuigou lobe history is an example of the deltaic lobe-building process and is the used to validate the model.

### 3. Methods

#### 3.1. Measuring Progradation of the Yellow River Delta

Satellite remote sensing data are used to document Yellow River delta and delta lobe progradation over the last ~45 years (Bi et al., 2014; Chu et al., 2006; Fan et al., 2006; Kong et al., 2015; Kong et al., 2015; van Gelder et al., 1994; Wang et al., 2006; Wu et al., 2017; Xu, 2003; Yu et al., 2011; Zhang et al., 2016, 2017). Previous studies focused on the radially averaged delta progradation rate, but a direct measure of lobe progradation rate is needed to validate the present numerical model. Eighty cloud-free Landsat (1–5, 7, and 8) sensor measurements from 1973 to 1997 are collected for this study. The Landsat 1, 2, and 3 MSS sensor Band 7 measurements ( $n = 31$ ) are manually georeferenced, and the coastline is traced to ~60-m accuracy. All other



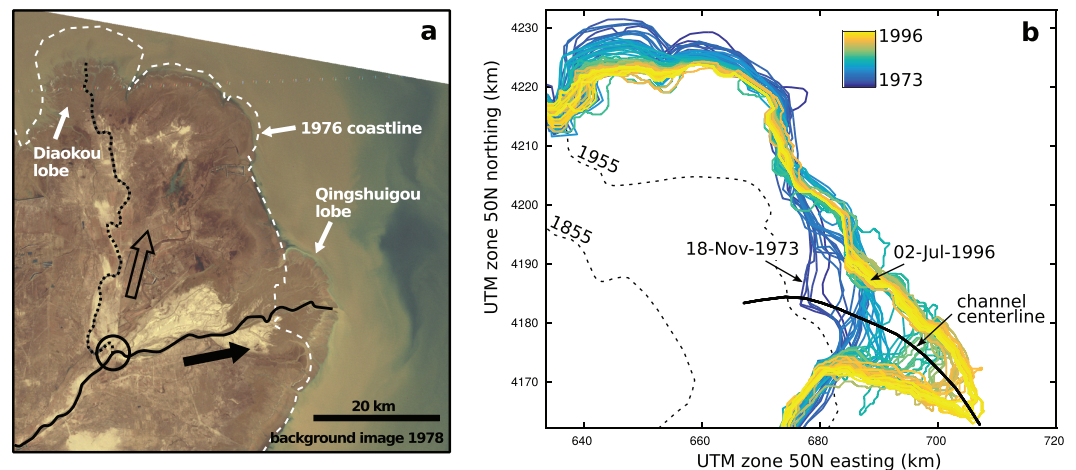


**Figure 4.** (a) Landsat 2 satellite composite image (1978) with superimposed coastline trace from a 1976 Landsat 2 image (white dashed line). In 1976, an engineered avulsion at the small open circle changed the channel course from the north (dotted line, open arrow) to the east (solid line, solid arrow). When compared to the 1976 coastline, the underlying satellite image shows retreat of the former delta lobe in the north (Diaokou lobe) and development of a new lobe to the east (Qingshuigou lobe); development of the Qingshuigou lobe continued without subsequent avulsion until 1996. (b) Coastline traces derived from historical record and satellite images. Traces from 1973 to 1982 are from manually georeferenced Landsat 1–3 sensor measurements. Traces from Landsat 4, 5, 7, and 8 are derived by automatic image processing (details and positional error information are included in text). Thick black line represents a portion of the channel centerline during the progradation of the Qingshuigou lobe.

satellite measurements (from Landsat 4, 5, 7, and 8; sensors TM/ETM/OLI+TIRS Band 7;  $n = 49$ ) are processed by computer script to derive the coastline location (supporting information S1). The 1855 and 1955 mapped coastline positions (Figure 2b) are also georeferenced and traced. Uncertainty in coastline position arises due to georeferencing error and tidal stage at the time of image acquisition. For Landsat measurements, georeferencing error is small with respect to effects of periodic tidal stage; as such, uncertainty is assigned a conservative value of  $\pm 3$  km for these measurements (supporting information S1). For historically mapped coastlines, there is a greater potential for mapping error, map distortion effects, and georeferencing errors to impact measurements; these coastlines are assigned an uncertainty value of  $\pm 15$  km. The 82 coastline traces document progradation of the subaerial Qingshuigou deltaic lobe (Figure 4b).

### 3.2. Model Design

The numerical model developed herein is a combination of an existing one-dimensional (1-D) numerical framework (e.g., Chatanantavet et al., 2012; Moran et al., 2017; Parker, 2004; Parker et al., 2008a, 2008b; Snyder et al., 2006) and a 2-D delta growth model (e.g., Parker, Paola, Whipple, & Mohrig, 1998; Parker, Paola, Whipple, Mohrig, Toro-Escobar, et al., 1998; Kim et al., 2009; (Figures 5a and 5b). In the model, sediment transport and deposition are coupled to fluid flow through the normal flow and backwater regions, to evolve the channel bed in time in 1-D. When a set of imposed avulsion criteria are met within the 1-D framework, mass is redistributed in a radially symmetric 2-D delta framework to mime natural deltaic processes occurring over multiple avulsion cycles.

Delta processes that occur over multiple lobe progradation and avulsion cycles are spatially and temporally averaged by the radially symmetric delta formulation. Conceptually, it is assumed that over a few avulsion cycles, fluvial processes will reach the entire delta topset surface (Ganti et al., 2014; Sun et al., 2002), a delta lobe will visit all locations along the delta coastline (Ganti et al., 2016b) and be reworked by coastal processes following abandonment. In this way, the model reproduces the long-term behavior of a prograding and aggrading delta. This radially symmetric formulation does not require specifying the location of the river channel or delta lobes in the 2-D framework, the number of delta lobes (Chadwick et al., 2019), or rates of coastal reworking (K. Ratliff, 2017; K. M. Ratliff et al., 2018). Overall, the model is most similar to Chadwick et al. (2019) but applies a different downstream boundary condition for lobe progradation, maintains a different formulation that accounts for multiple avulsion cycles, and emulates processes reworking a delta lobe upon abandonment (as opposed to stasis; Chadwick et al., 2019).

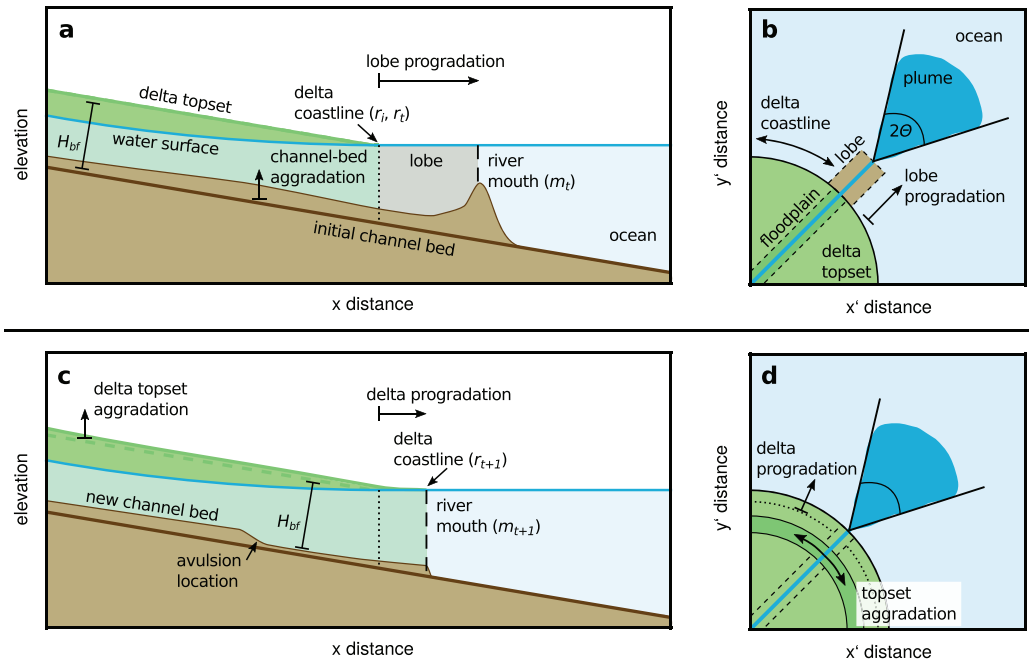


**Figure 5.** Schematic (not drawn to scale) depicting numerical model immediately prior to an avulsion in (a) the one-dimensional long profile, showing the subaerial delta topset, change in channel bed elevation (shaded brown area) from the initial channel bed to a bankfull flow depth below the topset (thick dark-brown line), water surface (blue line), the initial delta coastline position (which is also the initial mouth location before lobe progradation), and the current river mouth position and extent of lobe (shaded brown). (b) Planform depiction of the delta system for the same time as in Panel a (the long profile would be a slice down the 45° axis); the floodplain (shaded in dark green) and a developed lobe (shaded in brown) depict the model depositional area.  $\theta$  is the offshore-plume spreading angle, here set to 5° after Lamb et al. (2012). (c) Long profile and (d) planform schematic depicting numerical model immediately following an avulsion. Sediment in the delta lobe is redistributed along the delta front, and sediment deposited in the floodplain is redistributed axisymmetrically across the delta topset over the annulus area for each  $x$  coordinate, thereby prograding and aggrading the delta. The channel bed is linearly interpolated to a bankfull flow depth below the topset for locations downstream of the avulsion location.

The principles of fluid mass and momentum conservation are used to calculate changes in flow depth ( $H$ ) from the receiving basin, through the backwater region, and into the normal flow region upstream for a depth-averaged, gradually varied flow in the streamwise direction ( $x$ ) for a given volumetric water discharge ( $Q_w$ ):

$$\frac{dH}{dx} = \frac{S - C_f Fr^2}{(1 - Fr^2)} + \frac{Fr^2}{(1 - Fr^2)} \frac{H}{B} \frac{dB}{dx}, \quad (3)$$

where  $C_f = 0.001$  is the dimensionless coefficient of friction for the Yellow River (Ma et al., 2017),  $Fr^2 = Q_w^2 / g B^2 H^3$  is the Froude number for a rectangular channel,  $g$  is the gravitational acceleration constant, and  $B$  is the width of the flow, set by the channel width  $B_c$  in the confined fluvial portion of the model domain and increasing by  $dB/dx = 2 \tan \theta$ , where  $\theta = 5^\circ$  for the geometric approximation of a spreading plume beyond the river mouth, as measured relative to the flow centerline (supporting information S1; Chatanantavet et al., 2012; Lamb et al., 2012). A spreading plume abruptly increases the cross-sectional area of the flow beyond the river mouth such that the water surface elevation at the river mouth is relatively fixed regardless of the river discharge (e.g., Chatanantavet et al., 2012; Lamb et al., 2012; Rajaratnam, 1976; Rowland et al., 2009).

The sediment transport per-unit-flow width ( $q_s$ ) is calculated by

$$q_s = \sqrt{R g D_{50}^3} \frac{\alpha}{C_f} \tau_*^n, \quad (4)$$

where  $R$  is the submerged specific gravity of sediment,  $D_{50} = 90 \mu\text{m}$  is the median grain diameter of the bed material (Ma et al., 2017),  $\tau_* = C_f U^2 / R g D_{50}$  is the Shields number, and  $\alpha = 0.895$  and  $n = 1.678$  are adjusted coefficients to the generalized form of the Engelund and Hansen (1967) equation fit for the lower Yellow

River at the Lijin Hydrological Station (Figure 2a; Ma et al., 2017). Sediment transport is assumed to reach transport capacity and equilibrium (An et al., 2018) and comprises total bed-material load (i.e., washload is not modeled). The upstream model boundary is assumed to be at steady state such that the channel bed elevation is approximately fixed.

The long-term bed evolution is modeled using a simplified equation for sediment mass conservation (García, 2008; Paola & Voller, 2005; Swenson et al., 2000):

$$(1 - \lambda_p) \frac{\partial \eta}{\partial t} = - \frac{\partial Q_s}{\partial x} \frac{1}{B_e}, \quad (5)$$

where  $\eta$  is the channel bed elevation,  $t$  is time,  $\lambda_p = 0.4$  is the channel bed porosity,  $Q_s = q_s B_c$  is the sediment flux over the flow width, and  $B_e$  is the effective width of sediment deposition (Chatanantavet & Lamb, 2014), defined by a piecewise function representing the combined widths of the channel ( $B_c$ ), floodplain ( $B_f$ ), and/or delta lobe ( $B_o$ ) that is determined as follows:

$$B_e(x) = \begin{cases} B_c + B_f & : x \leq r \\ B_c + B_o & : r < x \leq m, \\ B_c & : x > m \end{cases} \quad (6)$$

where  $r$  denotes the edge of the delta topset and  $m$  is the mouth position at the end of the lobe. In this way, levee development is approximated by an area the width of  $B_f$  aggrading in-step with the channel bed. Values for depositional widths ( $B_c = 0.4$  km,  $B_f = 4$  km, and  $B_o = 9$  km) are measured from satellite for the Yellow River delta system (supporting information S1).

The initial channel bed slope is set as a constant value ( $S_0 = 6.4 \times 10^{-5}$ ), determined by water surface elevation measurements in the normal flow reach (supporting information S1); this value is consistent with other slopes reported for the Yellow River (Ganti et al., 2014; Chunhong et al., 2005). Subsidence for the lower Yellow River delta is rapid and spatially variable due to ground-fluid extraction (5–10 mm/year; Higgins et al., 2013); model subsidence is conservatively parameterized as a spatially constant rate of 5 mm/year. The slope of the receiving basin serves as a downstream boundary condition for a prograding lobe; in the model, the Bohai Sea slope is set to an order of magnitude lower than the channel ( $6.4 \times 10^{-6}$ ) for depths greater than 18 m (Wang et al., 2006; Yu, 2002).

At the onset, the model is configured such that the initial delta arclength (i.e., radially symmetric coastline length) is 80 km over the delta opening angle  $\Gamma = 90^\circ$ , approximately the Yellow River delta coastline length as measured in 1855 at the initiation of the Yellow River delta at its present location (Figures 2b and 5b; van Gelder et al., 1994). The delta topset initially has a constant slope, equal to the channel bed slope. Initial flow depth at the mouth ( $H_m$ ) is equal to the bankfull flow depth  $H_{bf} = 4.5$  m, which is calculated for a bankfull discharge of  $Q_{w,bf} = 3,000$  m<sup>3</sup>/s (Wang & Liang, 2000; Zheng et al., 2017). The model uses a grid spacing of 0.6 km over a 400-km domain and variable time stepping routine to maximize computational efficiency and numerical stability; the range of time steps is approximately 10 s to one quarter of a day. The model evolves repeatedly (solving equations (3)–(5)) and updates the channel bed profile.

Daily variations in water discharge are important for modeling the Yellow River system because the small bed-material grain size ( $D_{50} = 90$   $\mu$ m) and minimal channel form drag (Ma et al., 2017) enhance sediment transport such that geomorphically significant changes occur even for low discharges (Ma et al., 2017). Water discharge data from the Lijin Hydrological Station (river kilometer 100, as measured upstream from the river mouth) are used as a boundary condition. Three water discharge inputs are designed for the model. A data set of daily-averaged discharges from 1976 to 1996 is used to simulate lobe growth for testing the model by comparing to the development of the Qingshuigou lobe (Figure 6a). Another water discharge data set is produced by averaging daily measurements from a single calendar day of all years from 1950 to 2000 (Figure 6b); for example, all measurements from 1 January are averaged to produce the first value in the 365-day time series. With this calendar-mean input, bankfull discharge ( $Q_{w,bf} = 3,000$  m<sup>3</sup>/s) is nearly reached each year, while for the remainder of the year, the river experiences lower flows, averaging  $\sim 400$  m<sup>3</sup>/s. The calendar-mean input approximates the water discharge distribution for the Yellow River delta and is used to simulate delta evolution into the future under similar conditions. A third data set uses flooding discharge as an input parameter while holding the duration of the flood fixed (Figure 6c); this artificial discharge time series is designed to be similar to the calendar-mean discharge curve but allows for the

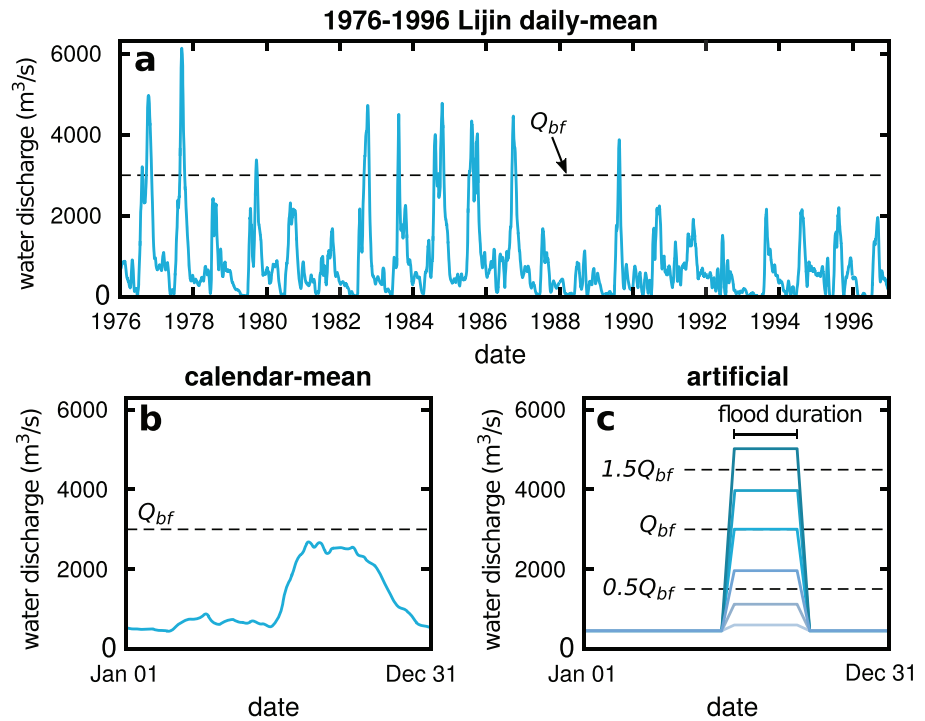


**Figure 6.** (a) Daily-average water discharge from 1976 to 1996 at Lijin. (b) Calendar-day average of daily-average water discharge from 1950 to 2000 at Lijin. (c) Artificial water discharge inputs. Dashed line in all plots is the lower Yellow River bankfull discharge,  $Q_{w,bf} = 3,000 \text{ m}^3/\text{s}$  (Wang & Liang, 2000; Zheng et al., 2017).

exploration of the effects of low-to-flood-flow disparity. To this end, the low-flow periods of the input time series have a constant discharge ( $400 \text{ m}^3/\text{s}$ ) and a flood discharge that varies in magnitude with respect to a bankfull discharge ( $Q_{w,\text{artificial flood}} = 500 \text{ to } 3,000 \text{ m}^3/\text{s}$ ).

The location of the river mouth is initially imposed where the delta topset intersects sea level (i.e., the extent of the subaerial delta). During model simulation, the location of the channel mouth is determined to be the most basinward location where the channel bed has aggraded such that the flow depth is less than the formative discharge depth ( $H_{\text{form}}$ ). Thus, flow in the spreading plume beyond the river mouth converts into channelized flow as the mouth and lobe prograde (i.e., equation (6) and Figures 5a and 5b). The treatment of lobe progradation is similar to Chadwick et al. (2019) and is different from previous work that uses a moving boundary formulation for the foreset wedge and fixes the location of plume spreading (Chatanantavet & Lamb, 2014; Chatanantavet et al., 2012). The formative discharge of the lower Yellow River is determined to be  $1,300 \pm 100 \text{ m}^3/\text{s}$ , based on the discharge with maximum geomorphic work potential, which is defined by the product of the frequency of flood recurrence and magnitude of associated sediment transport (e.g., Jerolmack & Brzinski, 2010; Wolman & Miller, 1960; see supporting information S1); the formative depth is calculated to be  $H_{\text{form}} = 2.6 \text{ m}$ . Thus, the flow depth at the mouth for most of the model run time is equal to the formative flow depth ( $H_m \approx H_{\text{form}}$ ). Following a change in the mouth location, the channel and effective depositional widths ( $B_c$  and  $B_e$ ) are updated appropriately.

An avulsion occurs in the model when sediment aggradation on the channel bed elevates the bankfull water surface ( $\eta + H_{bf}$ ) to a critical height (Chadwick et al., 2019; Ganti et al., 2016b, 2014, 2016a; Jerolmack & Mohrig, 2007; Mohrig et al., 2000; Moran et al., 2017; Ratliff et al., 2018). This aggradation creates channel instability by superelevation ( $\Delta Z$ ), which is calculated at each model node as the difference between the elevation of the radially symmetric delta topset ( $Z$ ) and the channel bed elevation:

$$\Delta Z(x) = \eta(x) + H_{bf} - Z(x). \quad (7)$$

This is equivalent to comparing the levee height to the average floodplain height or to other channel pathways on the floodplain, as it is assumed that levees grow in-step with the channel bed (e.g., Chadwick et al.,



2019; Ratliff et al., 2018). When the superelevation metric exceeds the critical aggradation threshold for avulsion ( $\Delta Z > \beta H_{bf}$ ; equation (2)), the avulsion setup threshold is reached. An avulsion must occur within the domain of the radially symmetric delta (as opposed to the delta lobe), thus ensuring a lobe-switching event. Finally, only one avulsion is permitted per flooding cycle; this restriction is necessary because the avulsion is executed instantaneously in model time and prevents multiple avulsions in a single flood event. If all of these three conditions are satisfied, then an avulsion is triggered at the appropriate spatial  $x$  coordinate at time  $t$ .

When an avulsion is triggered, the volume of sediment deposited within the lobe portion of the model domain is distributed along the entire delta coastline, thus prograding the delta (Figure 5d); the increase in delta radius is calculated according to mass conservation and is a function of the lobe volume, basin depth, and coastline length at the time of avulsion (supporting information S1). To aggrade the delta system before avulsion cycle  $n + 1$ , where  $n + 1$  is the cycle following the  $n$  avulsion cycle, the sediment deposited within the model floodplain at each  $x$  coordinate (i.e., equations (5) and (6)) during cycle  $n$  is redistributed axisymmetrically across the delta topset over an annulus area  $A(x)$ . The updated topset elevation is calculated for each  $x$  coordinate (Figure 5d):

$$Z_{n+1}(x) = Z_n(x) + \frac{\Delta\eta_n(x) \Delta x B_f}{A(x)}, \quad (8)$$

where  $\Delta\eta_n$  is the change in bed elevation during avulsion cycle  $n$ ,  $\Delta x$  is the  $x$ -coordinate grid spacing, and  $A = \pi/\Gamma_{\text{rad}}((L + \Delta x/2)^2 - (L - \Delta x/2)^2)$  is the area of an annulus at each  $x$  coordinate, where  $\Gamma_{\text{rad}}$  is the delta opening angle in units of radians and  $L$  is the  $x$ -coordinate distance from the delta apex. This method of redistributing lobe and floodplain sediment averages deltaic processes occurring over multiple lobe progradation and avulsion cycles. The formulation assumes that (1) deposition covers the entire delta topset and delta front after a few avulsion cycles (i.e., channels and lobes), and (2) physical processes reworking the deltaic deposits (e.g., waves and channel lateral migration) effectively redistribute sediment across the delta surface and front (Anthony, 2015; Chu et al., 2006; Ganti et al., 2016b; Reitz & Jerolmack, 2012). Under these assumptions, the radially symmetric formulation approximates the development of delta over multiple avulsion cycles and assumes that the resurfacing is uniform and no sediment is lost from the delta. This treatment of delta growth occurs instantaneously during the modeled avulsions, so development of the quasi-2-D deltaic system is due exclusively to floodplain and lobe sediment redistribution.

An avulsion marks the initiation of a new channel, which requires updating the bed to a new profile. Downstream of the avulsion location and extending to the delta coastline, the new channel bed is set to be one bankfull flow depth below the delta topset (Hajek & Edmonds, 2014; Mohrig et al., 2000); beyond the radially symmetric delta coastline, the bed is reset to the initial basin elevation (Figure 5c). Upstream of the avulsion location, the bed remains unchanged, which creates a step in the bed-elevation profile. A linear interpolation across 21 model nodes centered at the avulsion location ( $\sim 7$  km in each direction) smooths the step in bed elevation (Ganti et al., 2019) and is necessary for numerical stability.

To test the model, several runs are performed with variable boundary conditions. First, a validation run is conducted to compare model predictions to recorded lobe growth from the Qingshuigou lobe. The model is then run over multiple lobe-building cycles to evaluate the controls on channel bed aggradation patterns that set up avulsion timing and location. Specifically, model runs vary the superelevation avulsion setup threshold and the low-to-flood flow disparity, because these factors have been shown to impact the timing and location of avulsions (Chadwick et al., 2019; Ratliff, 2017, 2018).

## 4. Results

### 4.1. Measured Yellow River Delta Progradation

Yellow River delta progradation during the period from 1976 to 1996 (Qingshuigou lobe) is well-constrained based on satellite measurements. The 82 coastline positions are processed to derive a mean radius of the coastline over the imposed  $90^\circ$  range of the delta extent (Figure 7a, also displayed in Figure 3). The average deltaic radius increases through time; the data spanning from 1855 to the 1996 avulsion ( $n = 81$ ) are fit with a linear regression, yielding a delta progradation rate of  $0.26 \pm 0.02$  km/year (Figure 7a). This regression is strongly influenced by the historically mapped delta coastlines; excluding these from the regression yields an estimated rate of  $0.13 \pm 0.03$  km/year, which may be related to the installation of reservoir structures along the Yellow River course (H. Wang et al., 2010; S. Wang et al., 2015).

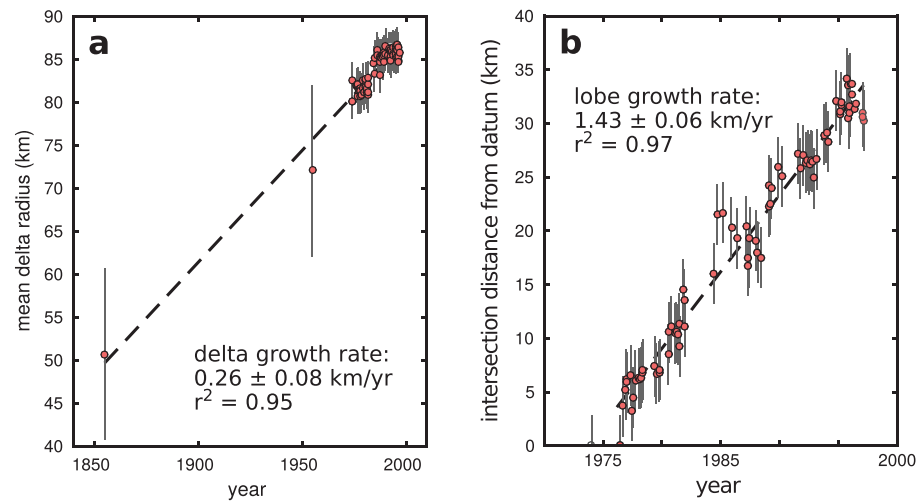


**Figure 7.** (a) Mean delta radius as measured from the datum of the city of Lijin, with best fit linear regression to data from 1855 to 1996. Note that this data set is also displayed in Figure 3a. (b) Lobe length as measured streamwise from the west end of the channel centerline mapped in Figure 4b, with a best fit linear regression to data from 1976 to 1996 (highlighted). This regression is a measure of the lobe progradation rate.

The Qingshuigou lobe growth is measured by tracking the intersection of a coastline and the channel centerline during lobe growth (Figure 4b, black line, and Figure 7b). This data set covers the time period of growth from 1976 to 1996 (i.e., the duration of Qingshuigou lobe growth,  $n = 75$ ) and yields a best fit line with an average lobe growth rate of  $1.43 \pm 0.06$  km/year for a total lobe length of  $\sim 30$  km (Figure 7b). This regression is a measure of the rate of linear lobe progradation. Numerous other authors have reported rates of Yellow River delta and delta lobe growth which generally agree with these findings (Table 1).

## 4.2. Model Results

### 4.2.1. Lobe Progradation Validation

The measured water discharge curve (Figure 6a) and the model parameterizations (Table 2) are used to simulate lobe growth over 21 years, thus replicating the time for the Qingshuigou lobe development (Figure 8). Over this period, the channel bed aggrades unevenly, and the locus of sedimentation occurs within the back-water region (Figure 8a). Initially, channel bed deposition is focused near the channel mouth, in the form of a vertically aggrading mouth bar. After a  $\sim 2$ -year period of no lobe progradation while the mouth bar

**Table 1**  
Compilation of Measured Delta Development Rates for the Yellow River Delta

Citation	Mean delta growth rate (km/year)	Unspecified lobe (km/year)	Qingshuigou lobe (km/year)	Avulsion node (km/year)
Qian et al. (1993)		$1.38 \pm 0.45^a$		
van Gelder et al. (1994)	0.15	1.5	$1.7 \pm 0.1^b$	
Li et al. (1999)		1.29		
Z. Y. Wang and Liang (2000)		$2.6^c$	2.3	
Xu (2003)			1.1–1.2	
Fan et al. (2006)		1–4	1.3	
Ganti et al. (2014)	$0.12 \pm 0.7$			$0.18 \pm 0.02$
Zheng et al. (2017)		2–3		
This study	$0.26 \pm 0.02$		$1.43 \pm 0.06$	$0.15 \pm 0.03$

*Note.* This study presents results that are similar to those measured by other researchers.

<sup>a</sup>Mean and standard deviation of preengineered lobes. <sup>b</sup>Annualized over measured record. <sup>c</sup>Average of two engineered lobes.

**Table 2**  
*Parameterization for Qingshuigou Lobe Progradation Validation Run and Long-Term Model Runs*

Parameter	Symbol	Model input	Units
Fluid density	$\rho$	1,000	kg/m <sup>3</sup>
Sed. density	$\rho_s$	2,650	kg/m <sup>3</sup>
Porosity	$\phi$	0.4	1
Domain length	$L$	400	km
Spatial step	$dx$	0.66	km
Time step	$dt$	8–21,600	s
Median grain size	$D_{50}$	90	$\mu\text{m}$
Initial bed slope	$S_0$	$6.4 \times 10^{-5}$	1
Bankfull discharge	$Q_{bf}$	3,000	m <sup>3</sup> /s
Formative discharge	$Q_{form}$	1,300	m <sup>3</sup> /s
Bankfull flow depth	$H_{bf}$	4.5	m
Formative flow depth	$H_{form}$	2.6	m
Backwater length scale	$\bar{L}_b$	40	km
Channel width	$B_c$	0.4	km
Floodplain width	$B_f$	4	km
Lobe width	$B_o$	9	km
Delta opening angle	$\Gamma$	90	°
Plume spreading angle	$\Theta$	5	°

aggrades, the delta mouth and lobe prograde unsteadily for 26 km (Figure 8). This yields an annualized rate of 1.24 km/year (Figure 8b), and regression to the mouth position over time yields a rate of 1.14 km/year (not plotted). A regression of the lobe position through time *after* the  $\sim 2$ -year period (i.e., when the model is not sensitive to the initial conditions) yields a rate of 0.94 km/year (Figure 8b). These rates compare well with satellite observations (Figure 7b), which show an average mouth progradation rate of  $1.43 \pm 0.06$  km/year.

The timing of the peak discharge from each year is extracted from Figure 6a and plotted as horizontal dashed lines in Figure 8b. Notably, pulses of mouth progradation coincide with the peak discharge of a year's flood, however, not every flood produces a pulse of mouth progradation. At the end of the model run, approximately 46% of the total sediment volume deposited in the model domain is part of the deltaic lobe, which is defined to include sediment deposited overbank in the lobe and in the channel bed of the lobe (i.e.,  $B_c + B_o$ ). When this depositional volume is normalized to account for the proportionately short length of the delta lobe with respect to the upstream channel length, 88% of sediment per unit length is deposited in the lobe (Figure 8c), with the remaining 12% of sediment resulting in channel and floodplain aggradation in the radially symmetric delta topset.

Deposited sediment volumes are calculated for discrete discharge bins over the duration of the validation run, deposition in the delta is separated from deposition in the lobe (i.e., exclusive of one another), and the volume in each bin is normalized to the cumulative input sediment flux for that discharge bin. Thus, comparing the fractions deposited in each model region for a dis-

charge bin indicates where most of the deposition occurs for a given water discharge range. Discharges above  $\sim 2,000$  m<sup>3</sup>/s are dominated by deposition in the delta lobe (red line, Figure 8c). Additionally, more sediment is deposited in the delta lobe for discharges above  $\sim 3,500$  m<sup>3</sup>/s than is input for the same time, indicating erosion of the channel bed and deposition of the sediment in the delta lobe.

The input water discharge curve exceeds 2,000 m<sup>3</sup>/s for only  $\sim 10\%$  of the duration of the model run, yielding sediment deposition in the upstream channel and floodplain for a majority of the time and in the delta lobe for a small fraction of time. Nonlinearity in water discharge to sediment flux relationships (e.g., equation (4)) means that though discharges  $\geq 2,000$  m<sup>3</sup>/s make up only 10% of duration of the run,  $\sim 42\%$  of total sediment input to the model domain is from this period. However,  $\sim 88\%$  (per unit length) of the total sediment is eventually deposited in the delta lobe (Figure 8). This mass balance accounting demonstrates that sediment is eroded from the channel bed during the largest floods in the simulation and redeposited in the delta lobe, despite the markedly short duration of these flood events.

#### 4.2.2. Channel Bed Aggradation Patterns Over Multiple Avulsion Cycles

The following model runs explore controls on channel bed sedimentation and deltaic lobe evolution patterns over multiple avulsion cycles; the model is evolved for 24 avulsion cycles (i.e., a sufficient number to characterize model behavior), and the three-avulsion-cycle spin-up period at the start of the run is discarded (Chadwick et al., 2019). The avulsion timing ( $T_A$ ), avulsion length ( $L_A$ ), and lobe length at time of avulsion ( $L_L$ ) are assessed by mean and standard deviation values.

Figure 9 shows results of a baseline long-term model run, which is useful to demonstrate how the model simulates delta evolution over multiple avulsion cycles, examine dynamic patterns of erosion and deposition within an avulsion cycle, and compare to other model runs and the historical record of Yellow River delta development. Water discharge repeats using the calendar-day average time series (Figure 6b), the avulsion setup threshold is  $0.5H_{bf}$ , and the remaining parameters are shown in Table 2. The avulsion time and length, and lobe length at the time of avulsion, are shown in Figures 9d–9f. After three lobe cycles (a model spin-up period), the time between avulsions and the lobe length vary about a mean value (Figure 9c). Each lobe cycle begins with a brief period during which a mouth bar aggrades before the lobe progrades (similar to Figure 8).

Over the duration of the model run, the delta system coastline has prograded approximately 40 km (Figure 9a), and the channel bed and delta topset have aggraded 2–3 m near the initial coastline position.

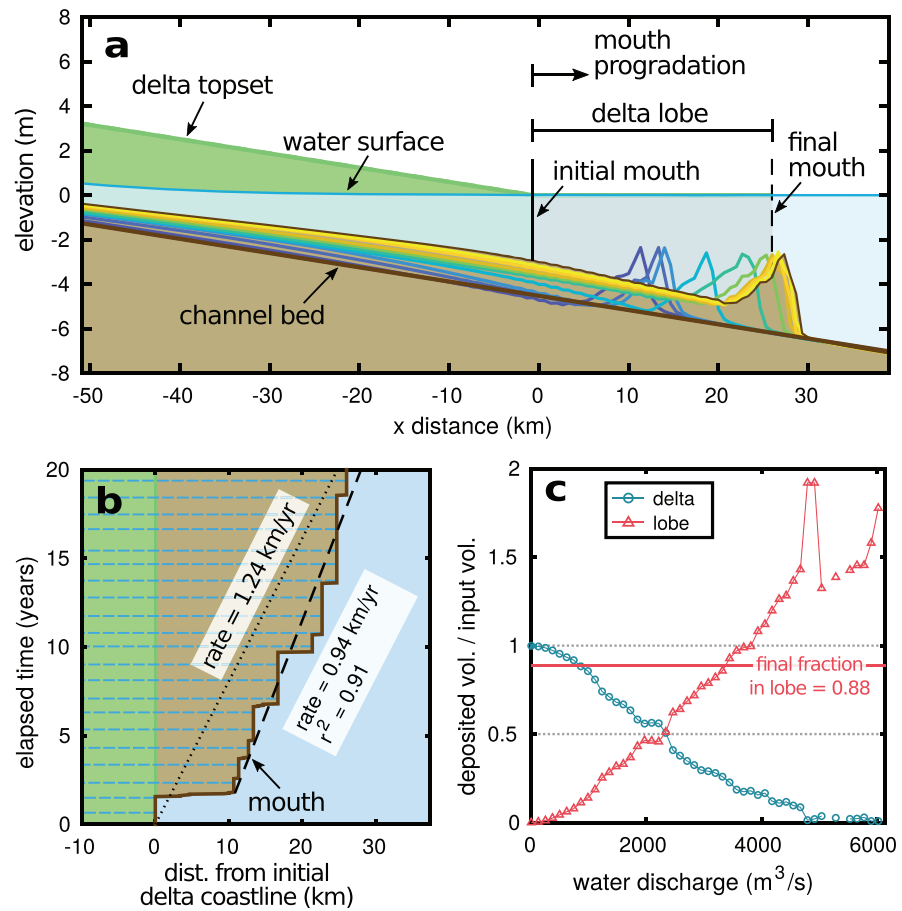


**Figure 8.** Model result from 1976 to 1996 Qingshuigou lobe progradation validation run. (a) Long profile depiction of channel bed evolution through 21 years, showing the aggradation of the bed followed by progradation of the mouth from blue to yellow lines denoting time progression. (b) No avulsion occurred during the model run, and the mouth location was prograded by ~26 km at an annualized rate of 1.24 km/year. A regression to the mouth location through time gives a rate of 0.94 km/year. Horizontal blue dashed lines denote timing of peak floods from hydrograph in Figure 6a. (c) Proportion of sediment deposited in delta or lobe region of the model, grouped into discrete discharge bins and normalized to the cumulative input sediment flux for that discharge bin. Discharges above ~2,000 m<sup>3</sup>/s are dominated by deposition in the delta lobe instead of the delta (red and blue lines, respectively). Discharges above ~3,500 m<sup>3</sup>/s show more sediment deposited than input, indicating erosion of the channel bed in the delta and redistribution to the delta lobe. At the end of the run, 88% of the total sediment input is deposited in the delta lobe (normalized per unit length).

The predicted avulsion length is  $L_A = 51.6 \pm 17.3$  km (mean  $\pm$  standard deviation) measured upstream from the channel mouth, which is  $1.3\bar{L}_b$ ; for all model runs, the backwater length scale is calculated from equation (1) using the formative discharge flow depth and initial channel bed slope ( $\bar{L}_b = (H_{\text{form}}/S) = (2.6 \text{ m}/6.4 \times 10^{-5}) \approx 40$  km). At the end of the model run, the channel bed long profile is convex up, a marker of avulsion setup due to hydrodynamic drawdown and variable water discharge (Chadwick et al., 2019). The predicted time between avulsions is  $T_A = 21.8 \pm 3.3$  year. Lobe length at the time of avulsion is  $L_L = 25.6 \pm 3$  km ( $0.6\bar{L}_b$ ).

The location of avulsion is shown in Figure 9c, where a periodic forward stepping of the node through time is apparent. The forward stepping predicted by a linear best fit is 0.06 km/year. Over the duration of the model run, the rate of radial delta system expansion slows; it is expected that the delta radius  $r$  scales with the square root of time  $t$  ( $r \approx t^{1/2}$ ; Carlson et al., 2018; Reitz et al., 2010; Swenson et al., 2000). However, the modeled radial growth rate is not better explained by a power law regression than a linear regression, which is simpler and offers a direct comparison with the record of Yellow River delta growth. The linear regression of delta system radial growth is 0.07 km/year (Figure 9c), though it is worth noting that the rate exceeds 0.1 km/year during early model development.



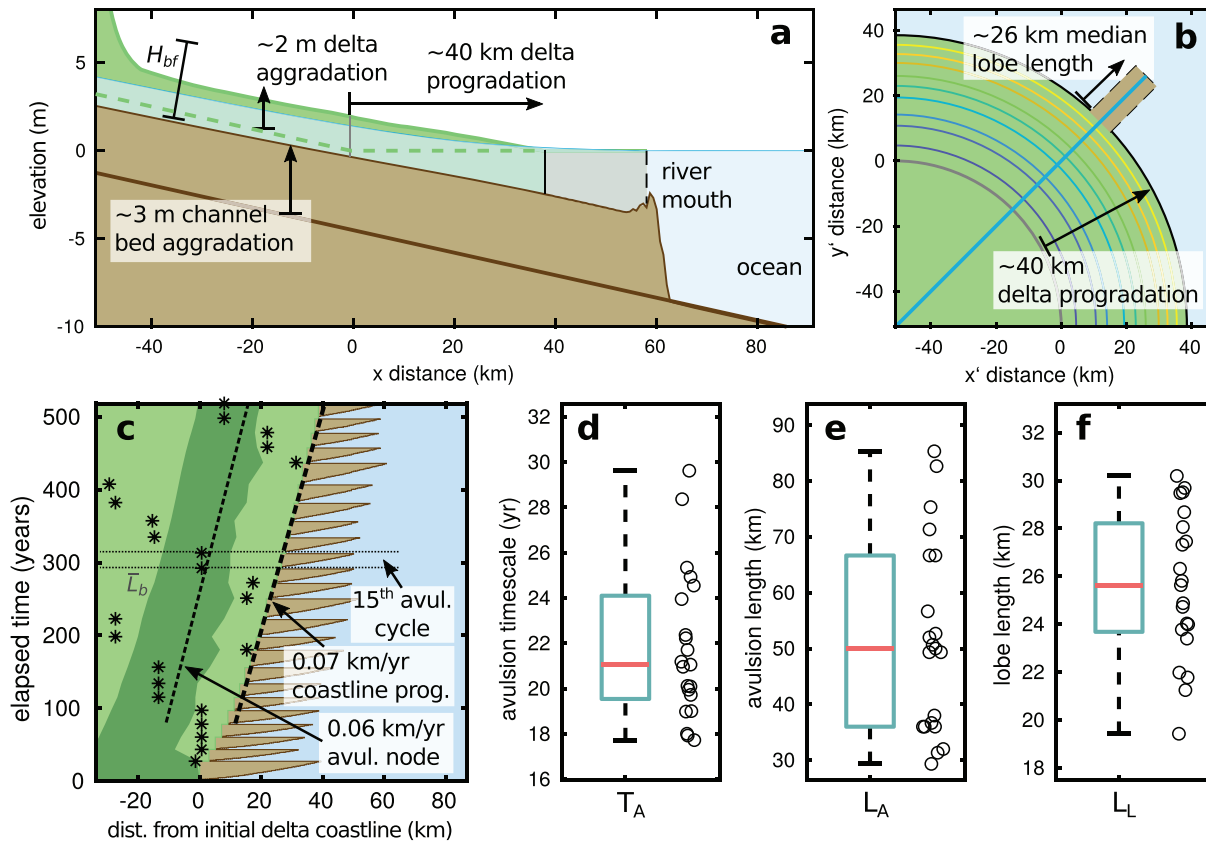


**Figure 9.** Model result from a 24-avulsion cycle run with calendar-averaged input water discharge data. (a) Long profile and (b) planform depiction of model immediately prior to the 24th avulsion; by which time the channel bed has aggraded  $\sim 3$  m over the model run, in step with the topset aggradation of  $\sim 2$  m. The delta coastline has prograded approximately 40 km; blue to yellow lines denote time progression. (c) Delta lobe and delta coastline progradation and avulsion location through time. Stars are timing and location of avulsions; shaded region denotes backwater region of model domain. Delta system growth occurs through repeating lobe progradation and avulsion cycles. Boxplots of avulsion statistics (excluding three-avulsion-cycle spin-up period) for (d) avulsion time ( $T_A$ ), (e) avulsion length ( $L_A$ ), and (f) lobe length at time of avulsion ( $L_L$ ).

#### 4.2.3. Variable Water Discharge and Avulsion Setup

Complementary to previous studies that indicate that the avulsion location is impacted by variable water discharge (Chatanantavet & Lamb, 2014; Chatanantavet et al., 2012; Lamb et al., 2012; Ganti et al., 2016a, 2016b), herein the downstream translation of the backwater region as a result of lobe progradation is explored to assess the impact on avulsion setup. Figure 10 explores the setup to the fifteenth avulsion (i.e., the fifteenth avulsion cycle) in the model run depicted in Figure 9, which is selected as a characteristic avulsion cycle ( $T_A = 21$  year,  $L_A = 49$  km or  $1.2\bar{L}_b$ ,  $L_L = 23$  km or  $0.6\bar{L}_b$ ). Figure 10a shows spatiotemporal changes in erosion and deposition through the avulsion cycle, and Figures 10d, 10c, and 10b examine morphodynamics during flood and subsequent low-flow cycles #6, #12, and #18, respectively (marked by brackets in Figure 10a).

At the onset of the avulsion cycle, the channel bed just upstream of the recent avulsion location is significantly eroded, and this sediment is deposited along the length of channel that has just been cut, downstream of the avulsion and to the mouth bar (Figure 10a). After about four flood cycles, the model oscillates between periods of erosion and deposition along most of the channel length, driving transient bed reworking in the backwater zone. For the remainder of the avulsion cycle, the locations of maximum sediment erosion and deposition are approximately 60 km upstream of the channel mouth and gradually translate downstream as the delta lobe progrades. Furthermore, the location of maximum bed deposition is near the upstream extent of the backwater region throughout the avulsion cycle (Figures 10b–10d). At the end of this cycle, an avulsion occurs just upstream of the backwater region ( $L_A \approx 1.0\bar{L}_b$ ), where superelevation is maximized due to a net aggrading channel bed (e.g., Chadwick et al., 2019).

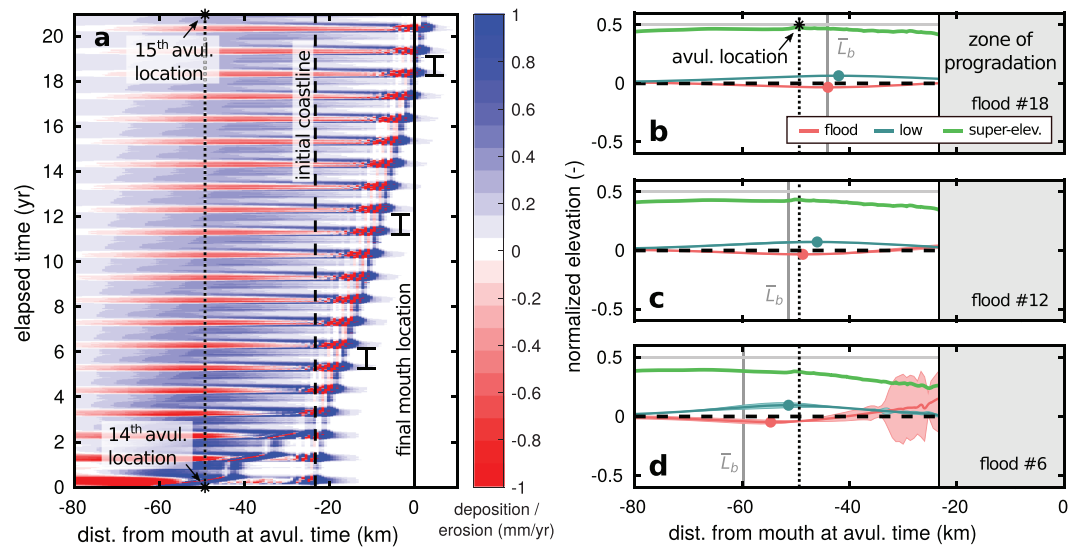


**Figure 10.** (a) Deposition and erosion rates through the setup to the fifteenth avulsion (i.e., the fifteenth avulsion cycle) in the model run depicted in Figure 9. Change in bed elevation for flood and subsequent low-flow cycles (b) #18, (c) #12, and (d) #6. Points mark the maximum deposition/erosion location for that flood cycle; shaded area is the standard deviation of the two cycles before and after (not visible in b and c).

#### 4.2.4. Avulsion Time and Length-Scale Controls

The avulsion setup threshold is varied over 10 model runs (Figures 11a–11c), because this condition has been shown to impact the location of deltaic avulsions (Ratliff, 2017). The avulsion time, avulsion length, and lobe length all increase nonlinearly with increasing setup threshold. The avulsion time (Figure 11a) increases from approximately 1 year for the smallest setup thresholds and tapers off to 60 year for a setup threshold of  $1.0H_{bf}$ . Avulsion length (Figure 11b) is approximately  $0.5\bar{L}_b$  for avulsion setup thresholds less than  $0.4H_{bf}$ , above which the avulsion length increases with the setup threshold and produces avulsions at  $3.0\bar{L}_b$  for a setup threshold of a full bankfull flow depth ( $1.0H_{bf}$ ). Lobe length (Figure 11c) behaves similarly to the avulsion length, increasing from zero length (i.e., no lobes developed) to lobes that are approximately as long as the backwater length scale ( $1.0\bar{L}_b$ ). For a setup threshold of  $0.4H_{bf}$ , the model predicts a lobe length of  $0.5\bar{L}_b$  and avulsions occurring at roughly the backwater length (Figures 11b and 11c).

The magnitude of the flood in the artificial water discharge input (Figure 6c) is varied for six model runs, and the avulsion setup condition is held fixed at  $0.5H_{bf}$  for all runs. These runs explore a similar condition to model runs by Chadwick et al. (2019) and examine the impact of variable water discharge on lobe progradation and avulsion timing and location. Bankfull discharge is  $Q_{w,bf} = 3,000 \text{ m}^3/\text{s}$  (Wang & Liang, 2000; Zheng et al., 2017), and so these runs explore a flooding discharge that ranges from  $500 \text{ m}^3/\text{s}$  ( $\ll Q_{w,bf}$ ) to  $5,000 \text{ m}^3/\text{s}$  ( $\gg Q_{w,bf}$ ); the low-flow duration of each artificial discharge input is  $400 \text{ m}^3/\text{s}$ . The outcome shows variable avulsion times, increasing abruptly from less than 10 year for artificial flood discharges  $\leq 1,000 \text{ m}^3/\text{s}$  ( $< 0.5Q_{w,bf}$ , Figure 6c) to  $\sim 30$  year for a flood discharge of  $5,000 \text{ m}^3/\text{s}$  (Figure 11d). Similarly, the avulsion length for artificial flood discharges  $\leq 1,000 \text{ m}^3/\text{s}$  is approximately  $0.25\bar{L}_b$  and increases by an order of magnitude (to  $2.5\bar{L}_b$ ) for a  $\sim 3\times$  increase in flood discharge (Figure 11e). The lobe length trend resembles the avulsion length pattern; it is zero for artificial flood discharges  $\leq 1,000 \text{ m}^3/\text{s}$  and increases linearly for ever increasing flood discharges (Figure 11f).

Avulsion time and length heat maps are produced by running the model over a range of avulsion setup threshold and flood discharge pairs, ranging from setup =  $0.2$  to  $0.6H_{bf}$  and flood discharge = calendar-mean input and  $2,000$  to  $3,500 \text{ m}^3/\text{s}$  (Figure 12). The mean time and length of avulsions following the model spin-up period are used to characterize avulsions for each setup-discharge pair. In gross, the avulsion time metric is largely controlled by the setup threshold, but the avulsion length metric is more evenly influenced by the combination of setup condition and flood discharge. Similar to the model runs varying the setup condition, an increase in setup threshold results in a nonlinear increase in both the avulsion time and length (Figure 12).

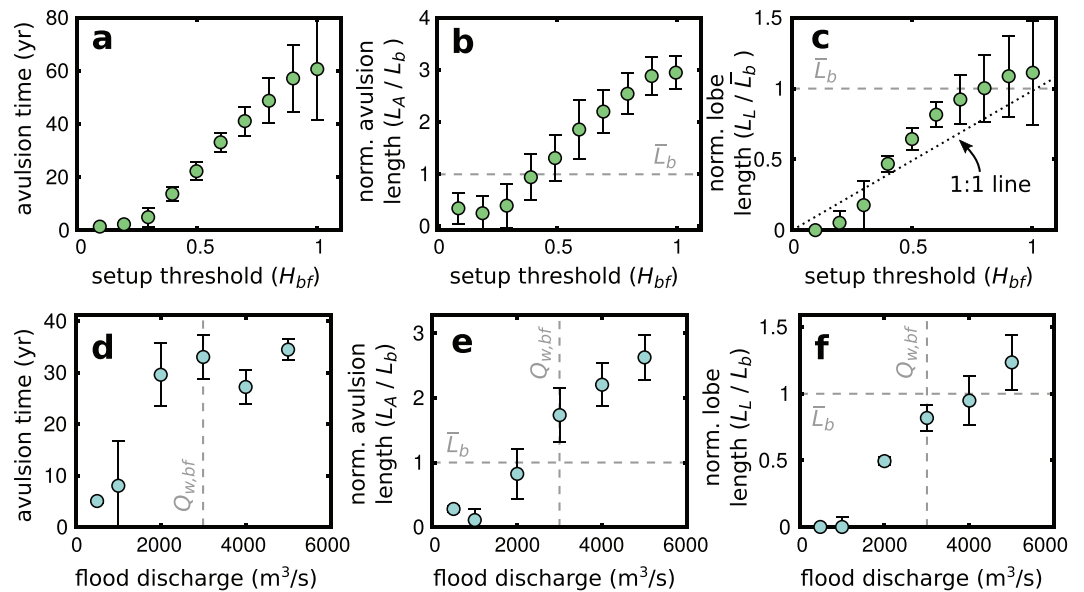


**Figure 11.** Avulsion time and length and lobe length at the time of avulsion for model runs which test the effect of change in (a–c) avulsion setup threshold and (d–f) flood intensity. Data points and error bars represent mean and standard deviation, respectively, of 21 avulsions following a three-avulsion-cycle spin-up period. In (a)–(c), increasing the setup threshold for avulsion produces a nonlinear increase in avulsion time and length and lobe length. The 1:1 line in (c) relates the setup threshold to lobe length through a scaling prediction (Chadwick et al., 2019; Ganti et al., 2014). In (d)–(f), small flood discharge runs ( $\leq 1,000 m^3/s$ ) separate from the higher flood discharge runs: Avulsion time and length are comparatively small, and no lobes develop. For larger flood discharges, avulsion time is longer but roughly constant, and avulsion length and lobe length increase linearly.

The predicted avulsion time and length for each condition pair are compared to the mean values tabulated for the Yellow River delta ( $T_{A,YR} = 7 \pm 2$  year and  $L_{A,YR} = 52.5 \pm 12.3$  km). The mean, standard deviation, and range of the Yellow River delta are denoted by the gray contours (Figure 12). The contours run on an angle across the heat maps, such that there are multiple setup-and-discharge pairs which produce avulsion times and lengths that are consistent with observations. However, the areas covered by the range of the data are nearly mutually exclusive, overlapping only for a setup conditions of  $0.2\text{--}0.3H_{bf}$  paired with flood discharges  $3,000\text{--}3,500 m^3/s$ .

## 5. Discussion

### 5.1. Lobe Progradation Validation

The validation run (Figure 8) demonstrates that the model produces values of lobe progradation ( $0.94$  km/year,  $1.24$  km/year annualized) that are consistent with measurements of the Qingshuigou lobe ( $1.43 \pm 0.06$  km/year; Figure 7). One particularly important model input is the delta lobe width, because the lobe progradation rate scales with the quotient of sediment volume input to the lobe and the average lobe cross-sectional area (i.e., average width times depth). The volume of sediment input is determined by hydraulics and a sediment transport prediction that is derived independently of lobe progradation observations (i.e., equations (3) and (4)). Despite uncertainty in values of sediment flux and basin depth, the model outcome using a single lobe width is effective to produce measured rates of delta lobe progradation. Potentially, relaxing the model assumption that washload (i.e., mud) does not contribute to lobe progradation might improve the predicted progradation rate. Note that in the measured record of lobe growth (Figure 7b), the Qingshuigou lobe immediately progrades with the avulsion in 1976. The brief spin-up period in the model occurs because deposition initiates on an approximately planar channel bed, and the mouth bar must aggrade before lobe progradation begins. This explains why the lobe progradation rate obtained by regression ( $0.94$  km/year) is slower than the measured rate. While the model underpredicts the rate and timing of lobe progradation, the model captures the integrated progradation rate (i.e., annualized,  $1.24$  km/year).

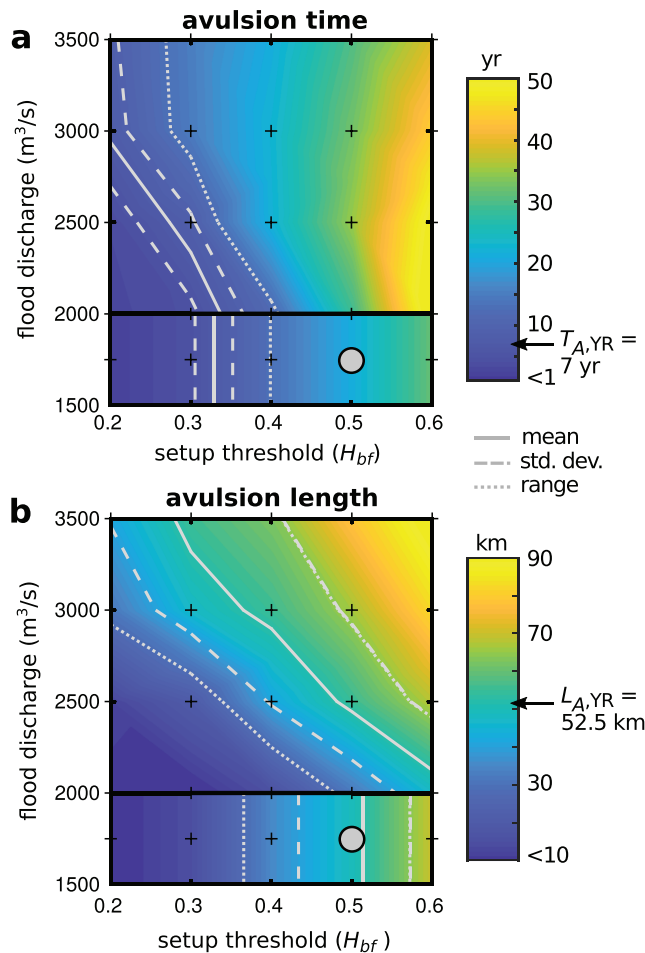


**Figure 12.** Heat maps of mean (a) avulsion time and (b) avulsion length for a range of setup and flood discharge pairs. Gray circle shows the model run in Figure 9. Gray lines denote the distribution of the Yellow River delta avulsion record data: mean (solid line,  $T_{A,YR} = 7 \pm 2$  year and  $L_{A,YR} = 52.5 \pm 12.3$  km),  $\pm 1$  standard deviation (dashed line), and the upper and lower bounds of the data range (dotted line).

In the validation run, the model predicts that the lobe progrades almost exclusively during floods (Figure 8b), because during these events, sediment deposition is primarily in the delta lobe and mouth bar (Figure 8c). The measured record of Qingshuigou lobe growth (Figure 7b) lacks the resolution to identify pulses of lobe progradation, making a high-resolution temporal comparison impossible, although a few satellite measurements record the lobe located well beyond the position predicted by the average measured growth rate, corresponding to years with historically large floods (e.g., 1983–1986; Figure 6), which could indicate pulses of lobe progradation coinciding with river flood events. Additionally, the deltaic lobe deposits have a pronounced mouth bar and steep foreset, consistent with the morphology of the modern Yellow River delta (Fan et al., 2006; Wang et al., 2016; Wu et al., 2015; Zheng et al., 2019).

Approximately 90% of the input discharge curve is below 2,000 m<sup>3</sup>/s, when sediment deposition is dominantly upstream of the lobe, yet roughly 88% of sediment per unit length is deposited in the delta lobe. This implies that sediment is intermittently stored in the channel during low-flow conditions and eroded with ensuing large floods, at which time sediment is relocated to the foreset (Chatanantavet & Lamb, 2014). Indeed, a large volume of sediment is redistributed to the delta lobe during floods, as is indicated by more sediment deposited in the lobe during a flood than is input to the model, a condition that requires supply from the eroded channel bed (Figure 8). Thus, hydrodynamic drawdown causes significant morphological change of the channel bed and delta system.

## 5.2. Spatially and Temporally Averaged Avulsion Cycle Dynamics

The radially symmetric delta formulation assumes that processes occurring over multiple avulsion cycles can be spatially and temporally averaged, which is different from other models simulating lobe-building and avulsion cycles (Chadwick et al., 2019; K. Ratliff, 2017; K. M. Ratliff et al., 2018). To test this assumption, the long-term baseline model run (Figure 9) is compared to the measured record of Yellow River delta development in Figure 3. The measured Yellow River delta coastline progradation rate for the last 150 years (0.26 km/year) compares to the modeled rate early in the run ( $> 0.1$  km/year; Figure 9c). Additionally, the mean avulsion length corresponds with the backwater length scale ( $L_A = 51.6 \pm 17.3 \approx \bar{L}_b = 40$  km), and the mean avulsion timescale is

within a factor of 3 of the measured avulsion timescale ( $T_A = 21.8 \pm 3.3$  year and  $T_{A,YR} = 7 \pm 2$  year). The modeled avulsion node forward-stepping and coastline progradation rates are subparallel, supporting the notion that forward stepping of the avulsion location is linked with the coastline position (Jerolmack, 2009; Ganti et al., 2014, 2016a, 2016b). The mismatch in coastline progradation and node forward-stepping rates is likely related to uncertainty in initial model configuration: The regional slope of the Yellow River delta could be up to a factor of 2 higher (Chunhong et al., 2005; Ganti et al., 2014), which potentially changes an important model boundary condition. An increased slope would lead to larger sediment flux reaching the delta and enhanced progradation; however, increasing slope would also modulate the basin depth that the lobe progrades into, which would lead to complex lobe and delta dynamics (Carlson et al., 2018). Regardless, the correspondence between model predictions and the Yellow River delta record suggests that over many avulsion cycles, spatial and temporal averaging of delta processes is justified.

At shorter time and space scales, the radially averaged formulation is susceptible to the effects of model initial conditions. In the baseline model run, the first few avulsions occur at the initial delta coastline (Figure 9c), where there is a slope break in the radially symmetric delta that persists until the topography is smoothed by the redistribution of floodplain material across the topset. Chadwick et al. (2019) observed that developing a more natural superelevation reference profile after multiple avulsion cycles eliminates geometric artifacts and these “geometric avulsions” that persist from the initial floodplain topography.



The radially symmetric delta formulation is unable to smooth the initial slope break without sediment redistributed to aggrade the topset. For example, in the model runs where the water discharge disparity is low (i.e.,  $Q_{w,flood} \leq 1,000$ ; Figures 11d–11f), sediment deposits within the delta backwater region rather than lobe, stymieing lobe progradation and causing an avulsion relatively rapidly that is located near the initial delta coastline (i.e., a geometric avulsion). Topset aggradation depends on the redistribution of floodplain sediment; hence, the small volume of sediment deposited during this relatively brief avulsion cycle yields little topset aggradation and the model initial conditions persist, priming yet another avulsion at the same location. A benefit of the Chadwick et al. (2019) model is that the initial topographic slope break is always smoothed after four avulsion cycles; in this way, the reference profile and channel bed aggradation are locked in-step. In the present model, fixing the sediment redistribution area  $A$  as function of distance from the delta apex  $L$  (equation (8)) yields a formulation very similar to Chadwick et al. (2019).

The radially symmetric delta system maintains a slope roughly parallel to the channel bed (Figure 9a). It might be intuited that the downstream increase in annulus area over which sediment is redistributed would steepen the slope over time, because sediment spread over a smaller area (upstream) aggrades faster. This would be true, if channel bed and floodplain aggradation during an avulsion cycle (i.e.,  $\Delta\eta$ ; equation (8)) were constant along the channel. However, the channel and floodplain aggrade more rapidly in the backwater region and downstream reaches of the channel, which overpowers the downstream increase in redistribution area  $A$ , and the radially symmetric delta topset autogenically maintains a slope similar to the channel bed. The downstream increase in  $A$  may not be compensated by a downstream increase in aggradation in all real-world delta systems though, and there may be cases where the delta system steepens in time.

The forward stepping of the avulsion location through time is not monotonous; there is a superimposed cycle of intermittent back stepping (Figure 9c) due to the radially symmetric delta formulation. Locations along the channel that receive proportionally more sediment during the avulsion cycle redistribute more material, and so the topset aggrades faster. Most sediment over an avulsion cycle is deposited downstream of the previous avulsion location, and so the topset aggrades faster there, raising the elevation to attain critical superelevation, and subsequent avulsions move upstream to where there has been slower topset aggradation and less aggradation is required to produce sufficient superelevation. When all upstream topset locations aggrade, the avulsion node jumps forward, and the back-stepping cycle repeats. This intermittent back-stepping behavior is consistent with a theory of delta evolution and scaling: Ganti et al. (2014) suggest that if the scale of lobe length approaches the backwater length scale, the avulsion node episodically steps forward, interspaced with times when the avulsion node is relatively stationary and the avulsion length varies around a mean value. In this perspective, the modeled intermittent avulsion location back stepping represents the period of relative stationarity of the avulsion node. An alternative formulation that prevents back stepping would be to aggrade the entire topset area evenly with each avulsion; however, this limits the development of autogenic topographic grading of the delta topset that is necessary for a backwater-mediated avulsion node (Chadwick et al., 2019).

### 5.3. Controls on Avulsion Setup and Timing

Previous research into the factors controlling deltaic avulsion setup has considered only a single avulsion cycle (e.g., Chatanantavet et al., 2012; Moran et al., 2017) or sought to identify the effect of flow variability on a preferential avulsion location (e.g., Chatanantavet & Lamb, 2014; Chadwick et al., 2019) or examined the relative influence of waves and/or tides and fluvial input on delta morphology and avulsion timing (Hoitink et al., 2017; Ratliff et al., 2018). The effect of lobe building on channel bed development under nonuniform flow conditions has been minimally explored as a control on avulsion location (Chadwick et al., 2019; Ratliff, 2017); herein, impacts of lobe progradation are examined in relation to avulsion setup.

The 24 avulsion cycle simulations explored above (Figures 9–11) affirm previous work regarding flow variability and a preferential avulsion location. Over the duration of the simulation in Figure 9, avulsions occur at a distance upstream of the mouth within a factor of 2 of the backwater length ( $L_A \approx L_b$ ), which is consistent with observations from natural deltas (Chadwick et al., 2019, 2012; Ganti et al., 2014, 2016a). During a single avulsion cycle (Figure 10), erosion, deposition, and lobe progradation interact to set up avulsion through superelevation. The location of preferential aggradation and superelevation in the present model is broader and not as well defined as in other studies (Chadwick et al., 2019; Ganti et al., 2016a). This leads to

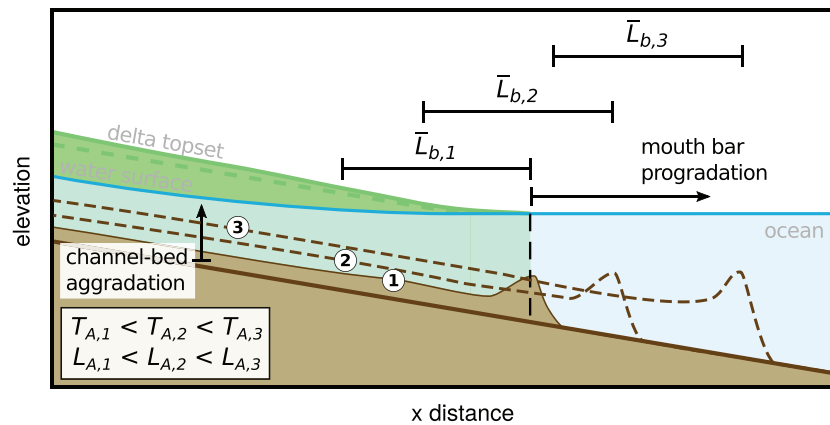


**Figure 13.** Sketch through backwater zone with channel bed depicted for three stages of delta development. Aggradation of the channel bed begins near the mouth bar and in the backwater region and proceeds until the lobe progrades. For an avulsion occurring without any lobe progradation (1), maximum aggradation and this avulsion would occur within the backwater reach, where low-flow deposition and flood-flow erosion set up a clear preferential node for avulsion (e.g., Chatanantavet et al., 2012; Chadwick et al., 2019; Ganti et al., 2016a). For a fixed sediment volume, deposition in the lobe reduces sediment deposited upstream, which slows (but does not halt), channel bed aggradation upstream. Thus, at some later time (2 and 3), when the avulsion setup threshold is reached, the location of avulsion is farther upstream. This results in larger avulsion time and length as a result of higher setup conditions and/or lobe progradation due to larger floods (i.e., Figure 11).

a large region of the delta which is nearly equally set for an avulsion, and hence, avulsions occur over most of the topset (Figure 10b).

This broad region of superelevation is a consequence of the prograding lobe, which is defined in the delta system via moving boundary coordinates. When the lobe progrades, aggradation in the backwater reach is reduced because sediment is routed to the deltaic lobe instead of being captured upstream to the channel bed. Conversely, progradation of the lobe lowers the fluvial slope and causes the channel system to shift the sediment depocenter upstream in order to reestablish its equilibrium slope (i.e., maintain constant sediment transport capacity) over the delta topset (Figure 13, Kim et al., 2006, 2009). The length scale of lobe progradation predicted herein is larger than documented in previous studies (Chadwick et al., 2019; Ganti et al., 2016a), and so the region of upstream aggradation is spread over a broader area. An important effect of shifting aggradation is to also move the avulsion location upstream, though the preferential avulsion length itself is modulated by variable water discharge (Chadwick et al., 2019).

Lobe progradation as an important control on avulsion location is documented with model runs that explore the control of avulsion setup threshold (Figure 11). Each of these runs has identical boundary conditions, and so sediment flux, per unit time, is fixed across the model runs. Hence, avulsion time increases for a constant sediment supply, as this condition requires more time to aggrade the channel bed (Figure 11a). The increased time to avulsion lets the mouth bar aggrade and also progrades the lobe. In turn, aggradation occurs upstream to maintain a constant fluvial slope (Figure 13). However, the interplay between lobe progradation and variable water discharge is nuanced: While the length of the lobe increases from zero to  $\sim 0.3\bar{L}_b$  for setup thresholds  $0.1\text{--}0.3H_{bf}$  (Figure 11c), the avulsion length remains fixed at  $\sim 0.5\bar{L}_b$ . In these runs, where the lobe length is small, the variable water discharge appears to be the most important factor determining where the avulsion occurs. This suggests that there is a trade-off point at a lobe length  $\sim 0.3\bar{L}_b$ , where deltaic avulsion location preference is set primarily by lobe progradation and upstream aggradation.

Similarly, the model runs with increasing artificial flood intensity highlight sensitivity to variable water discharge regimes, coupled with lobe progradation dynamics (Figures 11d–11f). Recent numerical modeling has demonstrated that low-to-flood-flow disparity is necessary to set up a consistent avulsion node located at roughly the backwater length ( $L_A \approx 1.0\bar{L}_b$ ; Chadwick et al., 2019). The low disparity model runs herein produce geometric avulsions (i.e.,  $Q_{w,\text{flood}} \leq 1,000$ , simulating a case similar to a constant discharge), because no delta lobe progrades and the model initial conditions are not smoothed. In contrast, larger flood discharges redistribute sediment from the channel bed to the delta lobe (e.g., Figure 8c), which simultaneously drives lobe progradation and avulsion setup due to low-to-flood-flow dynamics (e.g., Chadwick et al., 2019,

Figure 10). This codependence suggests that variable water discharge and lobe progradation must not be considered mutually exclusive in evaluating the timing and location of avulsions.

For a delta system that maintains a constant slope, the lobe progradation rate scales with the vertical aggradation rate upstream:

$$P \approx \frac{v_a}{S}, \quad (9)$$

where  $P$  is the lobe progradation rate (Chadwick et al., 2019; Ganti et al., 2014; Paola, 2000). Therefore, the length of a delta lobe at the time of avulsion is estimated by

$$L_L \approx P \cdot \bar{T}_A, \quad (10)$$

and by combining equation (9) with equations (1) and (2)

$$L_L \approx \beta \cdot \bar{L}_b, \quad (11)$$

where  $\beta$  is the avulsion setup threshold coefficient (Chadwick et al., 2019). The numerical experiments that vary the avulsion setup threshold explore this scaling prediction (Figures 11a–11c). For an avulsion setup threshold of  $1.0H_{bf}$ , the model predicts lobes that build out to approximately the backwater length ( $L_L = 1.0\bar{L}_b$ ) and avulsions that occur at  $\sim 3.0\bar{L}_b$  (Figure 11c). Indeed, for the full range of setup thresholds tested, the length of lobes is scaled to the avulsion setup threshold (1:1 line in Figure 11c). The development of this lobe scaling is an autogenic behavior of the model and arises only after the model spin-up period (during which lobes of more variable size are produced; e.g., Figure 9c). This is consistent with Chadwick et al. (2019), who suggest that it is necessary to bury initial model conditions before assessing autogenic dynamics like avulsion setup and timing.

Broadly, the model is consistent with field and experimental observations of delta avulsions and lobe-building processes: A setup threshold of  $0.4\text{--}0.5H_{bf}$  (Figures 11a–11c) produces avulsions at roughly the backwater length ( $L_A \approx 1.0\bar{L}_b$ ; Chatanantavet et al., 2012; Ganti et al., 2016a). Recent laboratory experiments that capture backwater-mediated deltaic avulsions, variable water discharge, and lobe progradation effects predict avulsions at  $\sim 0.5L_b$  for a setup level of  $\sim 0.3H_{bf}$  at the time of avulsion (Ganti et al., 2016b), which is generally consistent with the predictions made by the model (Figure 11b).

Overall, these results emphasize the importance of considering lobe size when evaluating avulsions in the field, from the rock record, or in experiments. If lobe development is small ( $L_L < 0.3\bar{L}_b$ ), then the avulsion setup is controlled mostly by variable water discharge. As the lobe length approaches the backwater length ( $L_L > 0.5\bar{L}_b$ ), the backwater region translates downstream substantially, and lobe progradation influences the avulsion location, though the node setup itself arises due to variable discharge dynamics (Chadwick et al., 2019). Therefore, in deltas where the lobe progrades to a moderate fraction of the backwater length ( $0.3\text{--}0.5\bar{L}_b$ ), the dynamic interplay between variable water discharge and lobe progradation sets the avulsion location, and a model capturing both processes is necessary to simulate development.

#### 5.4. Origin of Hydrodynamic and Geometric Avulsions

A similar relationship between setup threshold, lobe progradation, and avulsion length is documented in a recent numerical delta model by Ratliff (2017) and Ratliff et al. (2018). Their model produces “geometric” avulsions, which arise independently of variable water discharge or backwater hydrodynamics but still scale with the backwater length. Instead, geometric avulsions occur at a topographic slope break, defined by where a delta land surface (possessing a relatively flat gradient) protrudes from a terrestrial land surface (possessing a steeper gradient; Chadwick et al., 2019; K. Ratliff, 2017; K. M. Ratliff et al., 2018). Geometric avulsions arise due to the slope break: The floodplain elevation is nearly sea level at the topographic slope break, and because lobe progradation drives channel bed aggradation upstream (e.g., Figure 13), superelevation is reached most rapidly at the slope break (Chadwick et al., 2019; Ratliff, 2017).

The present model, as well as the Chadwick et al. (2019) model, couples floodplain development and channel bed aggradation in a manner that effectively smooths the topographic slope break and suppresses geometric avulsions after a few avulsion cycles (e.g., Figure 9). Furthermore, Chadwick et al. (2019) systematically document the importance of the reference floodplain profile used in calculating superelevation; using a more natural reference profile that developed after multiple avulsion cycles eliminated the geometric avulsions

in their model, and a backwater-scaled avulsion node emerged only with variable flows. This reference profile maintains a slope break in the Ratliff (2017) model, due to a weaker channel and floodplain coupling, and so geometric avulsions should persist in their model under either constant or variable flow regimes. Additionally, a steeper terrestrial land-surface slope in the Ratliff et al. (2018) model ( $1 \times 10^{-3}$ ) than in the present model ( $1 \times 10^{-5}$ ) produces a larger slope break, which requires a stronger channel-floodplain coupling to smooth.

The present model behaves similarly to the Ratliff (2017) model, insofar that lobe progradation is found to be a first-order control on the avulsion length and that initial avulsions occur at a topographic slope break between the delta and lobe. However, accounting for deltaic floodplain sedimentation in essence smooths the slope break and avulsion dynamics is then dictated by autogenic behavior of the fluvial system (i.e., discharge variability). Without this slope-break smoothing, geometric avulsions may occur at the backwater length scale, but the length scale is set by the distance from the slope break to the river mouth, which may be a function of delta age, regional slope, intensity of coastal processes, or model initial conditions.

### 5.5. Avulsion Triggering

An avulsion is dependent on a trigger, because a sustained levee breaching flow is necessary to establish a new channel course (Edmonds et al., 2009; Hajek & Wolinsky, 2012; Slingerland & Smith, 2004). Avulsion triggering may prove to be an important factor in natural systems, where flood discharge magnitude and frequency render avulsion timing stochastic. Ganti et al. (2014) demonstrate that rivers with highly variable flood intensity exhibit shorter avulsion timescales than expected by a “channel-fill timescale” that considers the superelevation of the channel (i.e., equation (2)). Two interpretations of this finding include (1) the variable flood intensity produces more focused aggradation at the avulsion node and/or (2) the channel does not require the level of superelevation expected to produce an avulsion.

In the model runs with increasing artificial flood intensity, the increase in sediment flux due to larger flood discharge does not reduce the avulsion timescale (Figure 11d), as might be expected from a mass conservation perspective. This is because increased sediment delivery occurs during flood discharge, with deposition almost exclusively in the delta lobe. Indeed, over a range of setup conditions and flood discharge inputs, the modeled avulsion timescale is insensitive to the variability of flood discharge (Figure 12), but the avulsion location is impacted as the lobe progrades and the channel bed aggrades upstream (i.e., Figure 13). In summary, increased sediment delivery due to flooding only marginally impacts aggradation rate and avulsion time.

All considered, this favors the latter interpretation, which explains why avulsion time measured for the Yellow River delta may be less than predicted: Higher flood intensity variability (and thus greater stage variability) produces more frequent overbank flooding at lower levels of superelevation, thereby reducing avulsion time (Ganti et al., 2014). Thus, the modeled avulsion times are best interpreted as upper limits to the range of expected avulsion times, though the trends observed are reliable. Forward models that predict avulsion timing and location could be better informed by flood intensity records. It also may be necessary to address flood stochasticity and avulsion trigger when modeling avulsion timing (e.g., Chadwick et al., 2019).

### 5.6. Comparison With Yellow River Deltaic Avulsion Record

The records of timing and location of Yellow River deltaic avulsions provide the opportunity to evaluate the appropriate avulsion setup threshold for this system by querying the model. The natural time and length scales of avulsions on the Yellow River delta are  $T_{A,YR} = 7 \pm 2$  year and  $L_{A,YR} = 52.5 \pm 12.3$  km. The avulsion length is closely matched for conditions across the range of setup-discharge pairs, and the avulsion time is best matched for an avulsion setup condition of  $0.2\text{--}0.3H_{bf}$  (gray contour lines, Figure 12). The setup threshold that best coincides with the avulsion time corresponds to an avulsion length of  $\leq 30$  km, which is shorter than observations.

Due to flood stochasticity and avulsion triggering uncertainty (section 5.5), the avulsion times calculated here are interpreted as upper limits. This puts a larger weight on the predicted avulsion length. The Yellow River delta is therefore interpreted to aggrade to  $0.3$  to  $0.5H_{bf}$  before avulsion, corresponding to an expected annual flood regime of  $2,500\text{--}3,500$  m<sup>3</sup>/s. These results are in general agreement with other field and laboratory research that estimate an avulsion setup condition between  $0.3$  and  $1.0H_{bf}$  (Ganti et al., 2014; Ganti et al., 2016b; Mohrig et al., 2000; Moran et al., 2017).



Superelevation on the modern Yellow River delta may be due to an upstream-migrating sediment wave, termed a “morphodynamic backwater” (Zheng et al., 2019), instead of the traditional hydrodynamic backwater (Ganti et al., 2016b). A morphodynamic backwater effect was not observed in any of the model runs herein, at least to the degree that it influenced the timing and location of avulsion. Zheng et al. (2019) favor such a morphodynamic backwater based on an observed longitudinal trend of decreasing erosion downstream, which they argue implies minimal hydrodynamic drawdown and thus precludes discharge-mediated setup of a preferential avulsion node. However, (1) erosion need not occur along the entire channel course during flood discharge (e.g., Figure 10), and (2) observations before and after a flood may record *net* aggradation, despite transient bed erosion in the backwater zone (e.g., Figure 10), because eroded sediment is immediately spent on progradation which lowers channel slope and drives aggradation upstream (e.g., Figure 13). Indeed, the progradation of the lobe and mouth bar is evidence of erosion of the channel bed at the mouth (Figure 15 in Zheng et al., 2019). A convex-up water surface long profile during floods would be indicative of hydrodynamic backwater setup (Chadwick et al., 2019), and the model presented herein reproduces such a pattern (e.g., Figure 8a and 9a). Interpreting the cause of modern avulsion setup is further complicated by the decades-long reduction in water discharge reaching the Yellow River delta (Wang et al., 2007), which has reduced the backwater length of the delta and likely shifted the preferred superelevation location downstream.

## 6. Conclusion

Fluvial-deltaic systems develop through repeated cycles of lobe building, initiated by the growth of a distributary channel and culminated by an avulsion. Predictive models for avulsion location and timing provide useful tools for understanding fluvial-deltaic processes, so as to facilitate interpretation of the sedimentary record and the future engineering of deltas. The quasi-2-D numerical model developed herein explicitly accounts for multiple deltaic lobe cycles and planform delta growth and thus provides insight into the processes that set up avulsion. It is found that the development of deltaic lobes drives upstream channel bed aggradation in response to reducing fluvial slope, as lobe progradation increases channel length. This upstream bed aggradation produces avulsions that occur less frequently and farther upstream than is realized in conditions that do not produce lobes. Specifically, when the delta lobe length is a moderate fraction of the backwater length ( $0.3\text{--}0.5\bar{L}_b$ ), the dynamic interplay between variable water discharge and lobe progradation sets the avulsion location, and a model capturing both processes is necessary. It is shown that increasing low-to-flood-flow disparity increases erosion at the mouth and drives lobe progradation, which in turn shifts the avulsion location upstream. Thus, the location of an avulsion is sensitive to the superelevation threshold, because larger lobes develop when the superelevation threshold is increased. The model parameter space is explored to produce a range of realistic avulsion time and length scales for the Yellow River delta system. Comparing the avulsion time and length scale of the Yellow River deltaic system to model predictions shows that this system aggrades to 30% to 50% of a bankfull flow depth before an avulsion.

## Acknowledgments

A. J. M., J. A. N., H. M., B. N. C., A. J. C., M. P. L., and G. P. acknowledge support from the National Science Foundation (NSF) EAR-1427262 Coastal SEES grant. A. J. M. was supported by a NSF Graduate Research Fellowship under Grant 1842494. A. J. C. was supported by the Resnick Sustainability Institute at Caltech. G. P. was supported by the NSF Grant EAR-1209402. The authors sincerely thank Vamsi Ganti and two anonymous reviewers for their thoughtful critique of this manuscript. The model code and supporting data can be obtained online ([https://github.com/amoodie/paper\\_resources/Moodie\\_deltaiclobebuilding](https://github.com/amoodie/paper_resources/Moodie_deltaiclobebuilding)).

## References

- Alsheikh, A. A., Ghorbanali, A., & Nouri, N. (2007). Coastline change detection using remote sensing. *International Journal of Environmental Science & Technology*, 4(1), 61–66. <https://doi.org/10.1007/BF03325962>
- Allison, M. A., & Meselhe, E. A. (2010). The use of large water and sediment diversions in the lower Mississippi River (Louisiana) for coastal restoration. *Journal of Hydrology*, 387(3–4), 346–360. <https://doi.org/10.1016/j.jhydrol.2010.04.001>
- An, C., Moodie, A. J., Ma, H., Fu, X., Zhang, Y., Naito, K., & Parker, G. (2018). Morphodynamic model of lower Yellow River: Flux or entrainment form for sediment mass conservation? *Earth Surface Dynamics*, 6(4), 989–1010. <https://doi.org/10.5194/esurf-6-989-2018>
- Anthony, E. J. (2015). Wave influence in the construction, shaping and destruction of river deltas: A review. *Marine Geology*, 361, 53–78. <https://doi.org/10.1016/j.margeo.2014.12.004>
- Ashworth, P. J., Best, J. L., & Jones, M. (2004). Relationship between sediment supply and avulsion frequency in braided rivers. *Geology*, 32(1), 21. <https://doi.org/10.1130/G19919.1>
- Assine, M. L. (2005). River avulsions on the Taquari megafan, Pantanal wetland, Brazil. *Geomorphology*, 70(3–4), 357–371. <https://doi.org/10.1016/j.geomorph.2005.02.013>
- Bi, N., Wang, H., & Yang, Z. (2014). Recent changes in the erosion-accretion patterns of the active Huanghe (Yellow River) delta lobe caused by human activities. *Continental Shelf Research*, 90, 70–78. <https://doi.org/10.1016/j.csr.2014.02.014>
- Brizga, S. O., & Finlayson, B. L. (1990). Channel avulsion and river metamorphosis: The case of the Thomson River, Victoria, Australia. *Earth Surface Processes and Landforms*, 15(5), 391–404. <https://doi.org/10.1002/esp.3290150503>
- Bryant, M., Falk, P., & Paola, C. (1995). Experimental study of avulsion frequency and rate of deposition. *Geology*, 23(4), 365. [https://doi.org/10.1130/0091-7613\(1995\)023<0365:ESOAFA>2.3.CO;2](https://doi.org/10.1130/0091-7613(1995)023<0365:ESOAFA>2.3.CO;2)
- Carlson, B., Piliouras, A., Muto, T., & Kim, W. (2018). Control of basin water depth on channel morphology and autogenic timescales in deltaic systems. *Journal of Sedimentary Research*, 88(9), 1026–1039. <https://doi.org/10.2110/jsr.2018.52>

- Chadwick, A. J., Lamb, M. P., Moodie, A. J., Parker, G., & Nittrouer, J. A. (2019). Origin of a preferential avulsion node on lowland river deltas. *Geophysical Research Letters*, 46, 4267–4277. <https://doi.org/10.1029/2019GL082491>
- Chatanantavet, P., & Lamb, M. P. (2014). Sediment transport and topographic evolution of a coupled river and river plume system: An experimental and numerical study. *Journal of Geophysical Research: Earth Surface*, 119, 1263–1282. <https://doi.org/10.1002/2013JF002810>
- Chatanantavet, P., Lamb, M. P., & Nittrouer, J. A. (2012). Backwater controls of avulsion location on deltas. *Geophysical Research Letters*, 39, L01402. <https://doi.org/10.1029/2011GL050197>
- Chu, Z. X., Sun, X. G., Zhai, S. K., & Xu, K. H. (2006). Changing pattern of accretion/erosion of the modern Yellow River (Huanghe) subaerial delta, China: Based on remote sensing images. *Marine Geology*, 227(1–2), 13–30. <https://doi.org/10.1016/j.margeo.2005.11.013>
- Chunhong, H., Yangui, W., Yanjing, Z., Yuling, T., Hongling, S., Cheng, L., et al. (2005). Case study on the Yellow River sedimentation. Beijing, China: International Research and Training Center on Erosion and Sedimentation.
- Coleman, J. M. (1988). Dynamic changes and processes in the Mississippi River delta. *Geological Society of America Bulletin*, 100(7), 999–1015. [https://doi.org/10.1130/0016-7606\(1988\)100h0999:DCAPITi2.3.CO;2](https://doi.org/10.1130/0016-7606(1988)100h0999:DCAPITi2.3.CO;2)
- Donselaar, M. E., Cuevas Gozalo, M. C., & Moyano, S. (2013). Avulsion processes at the terminus of low-gradient semi-arid fluvial systems: Lessons from the Río Colorado, Altiplano endorheic basin, Bolivia. *Sedimentary Geology*, 283, 1–14. <https://doi.org/10.1016/j.sedgeo.2012.10.007>
- Edmonds, D. A., Hoyal, D. C. J. D., Sheets, B. A., & Slingerland, R. L. (2009). Predicting delta avulsions: Implications for coastal wetland restoration. *Geology*, 37(8), 759–762. <https://doi.org/10.1130/G25743A.1>
- Engelund, F., & Hansen, E. (1967). *A monograph on sediment transport in alluvial streams*. Copenhagen, Denmark: Technisk Vorlag.
- Falcini, F., Piliouras, A., Garra, R., Guerin, A., Jerolmack, D. J., Rowland, J., & Paola, C. (2014). Hydrodynamic and suspended sediment transport controls on river mouth morphology. *Journal of Geophysical Research: Earth Surface*, 119, 1–11. <https://doi.org/10.1002/2013JF002831>
- Fan, H., Huang, H., Zeng, T. Q., & Wang, K. (2006). River mouth bar formation, riverbed aggradation and channel migration in the modern Huanghe (Yellow) River delta, China. *Geomorphology*, 74(1–4), 124–136. <https://doi.org/10.1016/j.geomorph.2005.08.015>
- Frazier, D. E. (1967). Recent deltaic deposits of the Mississippi River: Their development and chronology. *Transactions of the Gulf Coast Association of Geological Societies*, 27, 287–315.
- Ganti, V., Chadwick, A. J., Hassenruck-Gudipati, H. J., Fuller, B. M., & Lamb, M. P. (2016a). Experimental river delta size set by multiple floods and backwater hydrodynamics. *Science Advances*, 2(5), e1501768–e1501768. <https://doi.org/10.1126/sciadv.1501768>
- Ganti, V., Chadwick, A. J., Hassenruck-Gudipati, H. J., & Lamb, M. P. (2016b). Avulsion cycles and their stratigraphic signature on an experimental backwater-controlled delta: Backwater-controlled avulsion cycles. *Journal of Geophysical Research: Earth Surface*, 121, 1651–1675. <https://doi.org/10.1002/2016JF003915>
- Ganti, V., Chu, Z., Lamb, M. P., Nittrouer, J. A., & Parker, G. (2014). Testing morphodynamic controls on the location and frequency of river avulsions on fans versus deltas: Huanghe (Yellow River), China: Avulsion drivers on fans versus deltas. *Geophysical Research Letters*, 41, 7882–7890. <https://doi.org/10.1002/2014GL061918>
- Ganti, V., Lamb, M. P., & Chadwick, A. J. (2019). Autogenic erosional surfaces in fluvio-deltaic stratigraphy from floods, avulsions and backwater hydrodynamics. *Journal of Sedimentary Research*, 89, 815–832.
- García, M. H. (2008). Ch 2: Sediment transport and morphodynamics. *Sedimentation engineering processes, measurements, modeling, and practice* (pp. 21–163). Reston, VA: American Society of Civil Engineers.
- Hajek, E. A., & Edmonds, D. A. (2014). Is river avulsion style controlled by floodplain morphodynamics? *Geology*, 42(3), 199–202. <https://doi.org/10.1130/G35045.1>
- Hajek, E. A., & Wolinsky, M. A. (2012). Simplified process modeling of river avulsion and alluvial architecture: Connecting models and field data. *Sedimentary Geology*, 257–260, 1–30. <https://doi.org/10.1016/j.sedgeo.2011.09.005>
- Heller, P. L., & Paola, C. (1996). Downstream changes in alluvial architecture: An exploration of controls on channel-stacking patterns. *SEPM Journal of Sedimentary Research*, 66, 297–306. <https://doi.org/10.1306/D4268333-2B26-11D7-8648000102C1865D>
- Higgins, S., Overeem, I., Tanaka, A., & Syvitski, James P. M. (2013). Land subsidence at aquaculture facilities in the Yellow River delta, China. *Geophysical Research Letters*, 40, 3898–3902. <https://doi.org/10.1002/grl.50758>
- Hoitink, A. J. F., Wang, Z. B., Vermeulen, B., Huismans, Y., & Kästner, K. (2017). Tidal controls on river delta morphology. *Nature Geoscience*, 10(9), 637–645. Retrieved 2019-04-30, from <http://www.nature.com/articles/ngeo3000> <https://doi.org/10.1038/ngeo3000>
- Hoyal, D. C. J. D., & Sheets, B. A. (2009). Morphodynamic evolution of experimental cohesive deltas. *Journal of Geophysical Research*, 114, F02009. <https://doi.org/10.1029/2007JF000882>
- Jain, V., & Sinha, R. (2004). Fluvial dynamics of an anabranching river system in Himalayan foreland basin, Bagmati River, north Bihar plains, India. *Geomorphology*, 60(1–2), 147–170. <https://doi.org/10.1016/j.geomorph.2003.07.008>
- Jerolmack, D. J. (2009). Conceptual framework for assessing the response of delta channel networks to Holocene sea level rise. *Quaternary Science Reviews*, 28(17–18), 1786–1800. <https://doi.org/10.1016/j.quascirev.2009.02.015>
- Jerolmack, D. J., & Brzinski, T. A. (2010). Equivalence of abrupt grain-size transitions in alluvial rivers and eolian sand seas: A hypothesis. *Geology*, 38(8), 719–722. <https://doi.org/10.1130/G30922.1>
- Jerolmack, D. J., & Mohrig, D. (2007). Conditions for branching in depositional rivers. *Geology*, 35(5), 463. <https://doi.org/10.1130/G23308A.1>
- Jerolmack, D. J., & Swenson, J. B. (2007). Scaling relationships and evolution of distributary networks on wave-influenced deltas. *Geophysical Research Letters*, 34, L23402. <https://doi.org/10.1029/2007GL031823>
- Jones, L. S., & Harper, J. T. (1998). Channel avulsions and related processes, and large-scale sedimentation patterns since 1875, Rio Grande, San Luis Valley, Colorado. *Geological Society of America Bulletin*, 110(4), 411–421. [https://doi.org/10.1130/0016-7606\(1998\)110h0411:CAARPAi2.3.CO;2](https://doi.org/10.1130/0016-7606(1998)110h0411:CAARPAi2.3.CO;2)
- Kim, W., Dai, A., Muto, T., & Parker, G. (2009). Delta progradation driven by an advancing sediment source: Coupled theory and experiment describing the evolution of elongated deltas. *Water Resources Research*, 45, W06428. <https://doi.org/10.1029/2008WR007382>
- Kim, W., & Jerolmack, D. J. (2008). The pulse of calm fan deltas. *The Journal of Geology*, 116(4), 315–330. <https://doi.org/10.1086/588830>
- Kim, W., Paola, C., Swenson, J. B., & Voller, V. R. (2006). Shoreline response to autogenic processes of sediment storage and release in the fluvial system. *Journal of Geophysical Research*, 111, F04013. <https://doi.org/10.1029/2006JF000470>
- Kong, D., Miao, C., Borthwick, Alistair G. L., Duan, Q., Liu, H., Sun, Q., et al. (2015). Evolution of the Yellow River Delta and its relationship with runoff and sediment load from 1983 to 2011. *Journal of Hydrology*, 520, 157–167. <https://doi.org/10.1016/j.jhydrol.2014.09.038>

- Kong, D., Miao, C., Wu, J., Jiang, L., & Duan, Q. (2015). Bi-objective analysis of water-sediment regulation for channel scouring and delta maintenance: A study of the lower Yellow River. *Global and Planetary Change*, 133, 27–34. <https://doi.org/10.1016/j.gloplacha.2015.07.007>
- Lamb, M. P., Nittrouer, J. A., Mohrig, D., & Shaw, J. (2012). Backwater and river plume controls on scour upstream of river mouths: Implications for fluvio-deltaic morphodynamics. *Journal of Geophysical Research*, 117, F01002. <https://doi.org/10.1029/2011JF002079>
- Lee, J.-s., & Jurkevich, I. (1990). Coastline detection and tracing in SAR images. *IEEE Transactions on Geoscience and Remote Sensing*, 28(4), 662–668. <https://doi.org/10.1109/TGRS.1990.572976>
- Li, P., Yuan, J., Liu, L., & Fu, M. (1999). Vulnerability assessment of the Yellow River Delta to predicted climate change and sea level rise. Tech. Rep. No. Supervising Scientist Report 149.
- Liu, F., Chen, S., Peng, J., & Chen, G. (2012). Temporal variations of water discharge and sediment load of Huanghe River, China. *Chinese Geographical Science*, 22(5), 507–521. <https://doi.org/10.1007/s11769-012-0560-y>
- Lynds, R. M., Mohrig, D., Hajek, E. A., & Heller, P. L. (2014). Paleoslope reconstruction in sandy suspended-load-dominant rivers. *Journal of Sedimentary Research*, 84, 825–836. <https://doi.org/10.2110/jsr.2014.60>
- Ma, H., Nittrouer, J. A., Naito, K., Fu, X., Zhang, Y., Moodie, A. J., et al. (2017). The exceptional sediment load of fine-grain dispersal systems: Example of the Yellow River, China, 3, 7. <https://doi.org/10.1126/sciadv.1603114>
- Mariotti, G., Falcini, F., Geleynse, N., Guala, M., Sun, T., & Fagherazzi, S. (2013). Sediment eddy diffusivity in meandering turbulent jets: Implications for levee formation at river mouths. *Journal of Geophysical Research: Earth Surface*, 118, 1908–1920. <https://doi.org/10.1002/jgrf.20134>
- Martin, J., Sheets, B., Paola, C., & Hoyal, D. (2009). Influence of steady base-level rise on channel mobility, shoreline migration, and scaling properties of a cohesive experimental delta. *Journal of Geophysical Research*, 114, F03017. <https://doi.org/10.1029/2008JF001142>
- McCarthy, T. S., Ellery, W. N., & Stanistreet, I. G. (1992). Avulsion mechanisms on the Okavango fan, Botswana: The control of a fluvial system by vegetation. *Sedimentology*, 39(5), 779–795. <https://doi.org/10.1111/j.1365-3091.1992.tb02153.x>
- Mohrig, D., Heller, P. L., Paola, C., & Lyons, W. J. (2000). Interpreting avulsion process from ancient alluvial sequences: Guadalope-Matarranya system (northern Spain) and Wasatch Formation (western Colorado). *Geological Society of America Bulletin*, 112(12), 1787–1803.
- Moran, K. E., Nittrouer, J. A., Perillo, M. M., Lorenzo-Trueba, J., & Anderson, J. B. (2017). Morphodynamic modeling of fluvial channel fill and avulsion time scales during early Holocene transgression, as substantiated by the incised valley stratigraphy of the Trinity River, Texas: Modeling of channel fill and avulsions. *Journal of Geophysical Research: Earth Surface*, 122, 215–234. <https://doi.org/10.1002/2015JF003778>
- Nittrouer, J. A., Shaw, J., Lamb, M. P., & Mohrig, D. (2012). Spatial and temporal trends for water-flow velocity and bed-material sediment transport in the lower Mississippi River. *Geological Society of America Bulletin*, 124(3–4), 400–414. <https://doi.org/10.1130/B30497.1>
- Nittrouer, J. A., & Viparelli, E. (2014). Sand as a stable and sustainable resource for nourishing the Mississippi River delta. *Nature Geoscience*, 7(5), 350–354. <https://doi.org/10.1038/ngeo2142>
- Pang, J. Z., & Si, S. H. (1979). Evolution of the Yellow River mouth: I. Historical shifts. *Oceanologia et Limnologia Sinica*, 10(2), 136–141.
- Paola, C. (2000). Quantitative models of sedimentary basin filling: Quantitative models of sedimentary basin filling. *Sedimentology*, 47, 121–178. <https://doi.org/10.1046/j.1365-3091.2000.00006.x>
- Paola, C., & Mohrig, D. (1996). Palaeohydraulics revisited: Palaeoslope estimation in coarse-grained braided rivers. *Basin Research*, 8(3), 243–254. <https://doi.org/10.1046/j.1365-2117.1996.00253.x>
- Paola, C., Straub, K., Mohrig, D., & Reinhardt, L. (2009). The “unreasonable effectiveness” of stratigraphic and geomorphic experiments. *Earth-Science Reviews*, 97(1–4), 1–43. <https://doi.org/10.1016/j.earscirev.2009.05.003>
- Paola, C., Twilley, R. R., Edmonds, D. A., Kim, W., Mohrig, D., Parker, G., et al. (2011). Natural processes in delta restoration: Application to the Mississippi Delta. *Annual Review of Marine Science*, 3(1), 67–91. <https://doi.org/10.1146/annurev-marine-120709-142856>
- Paola, C., & Voller, V. R. (2005). A generalized Exner equation for sediment mass balance. *Journal of Geophysical Research*, 110, F04014. <https://doi.org/10.1029/2004JF000274>
- Parker, G. (2004). E-book: 1D sediment transport morphodynamics with applications to rivers and turbidity currents. E-book. Available at: [http://hydrolab.illinois.edu/people/parkerg/morphodynamics\\_e-book.htm](http://hydrolab.illinois.edu/people/parkerg/morphodynamics_e-book.htm)
- Parker, G., Muto, T., Akamatsu, Y., Dietrich, W. E., & Wesley Lauer, J. (2008a). Unravelling the conundrum of river response to rising sea-level from laboratory to field. Part I: Laboratory experiments. *Sedimentology*, 55(6), 1643–1655. <https://doi.org/10.1111/j.1365-3091.2008.00961.x>
- Parker, G., Muto, T., Akamatsu, Y., Dietrich, W. E., & Wesley Lauer, J. (2008b). Unravelling the conundrum of river response to rising sea-level from laboratory to field. Part II. The Fly-Strickland River system, Papua New Guinea. *Sedimentology*, 55(6), 1657–1686. <https://doi.org/10.1111/j.1365-3091.2008.00962.x>
- Parker, G., Paola, C., Whipple, K. X., & Mohrig, D. (1998). Alluvial fans formed by channelized fluvial and sheet flow. I: Theory. *Journal of Hydraulic Engineering*, 124(10), 985–995. [https://doi.org/10.1061/\(ASCE\)0733-9429\(1998\)124:10\(985\)](https://doi.org/10.1061/(ASCE)0733-9429(1998)124:10(985))
- Parker, G., Paola, C., Whipple, K. X., Mohrig, D., Toro-Escobar, C. M., Halverson, M., & Skoglund, T. W. (1998). Alluvial fans formed by channelized fluvial and sheet flow. II: Application. *Journal of Hydraulic Engineering*, 124(10), 996–1004. [https://doi.org/10.1061/\(ASCE\)0733-9429\(1998\)124:10\(996\)](https://doi.org/10.1061/(ASCE)0733-9429(1998)124:10(996))
- Peyronnin, N., Green, M., Richards, C. P., Owens, A., Reed, D., Chamberlain, J., et al. (2013). Louisiana’s 2012 coastal master plan: Overview of a science-based and publicly informed decision-making process. *Journal of Coastal Research*, 67, 1–15. <https://doi.org/10.2112/SIn67n1.1>
- Qian, Y. Y., Ye, W. C., & Zhou, W. C. (1993). Channel process of the Lower Yellow River in relation to water and sediment changes. *Publishing House for Construction Material Industry, Beijing*, 160–200.
- Rajaratnam, N. (1976). *Turbulent jets*, Developments in water science. Amsterdam; New York: Elsevier Scientific Pub. Co.
- Ratliff, K. (2017). From the river to the sea: Modeling coastal river, wetland, and shoreline dynamics (Doctoral Dissertation), Duke University.
- Ratliff, K. M., Hutton, Eric H. W., & Murray, A. Brad (2018). Exploring wave and sea level rise effects on delta morphodynamics with a coupled river ocean model. *Journal of Geophysical Research: Earth Surface*, 123, 2887–2900. <https://doi.org/10.1029/2018JF004757>
- Reitz, M. D., & Jerolmack, D. J. (2012). Experimental alluvial fan evolution: Channel dynamics, slope controls, and shoreline growth. *Journal of Geophysical Research*, 117, F02021. <https://doi.org/10.1029/2011JF002261>
- Reitz, M. D., Jerolmack, D. J., & Swenson, J. B. (2010). Flooding and flow path selection on alluvial fans and deltas. *Geophysical Research Letters*, 37, L06401. <https://doi.org/10.1029/2009GL041985>

- Ren, M.-e., & Walker, H. J. (1998). Environmental consequences of human activity on the Yellow River and its delta, China. *Physical Geography*, 19(5), 421–432.
- Richards, K., Chandra, S., & Friend, P. (1993). Avulsive channel systems: Characteristics and examples. *Geological Society, London, Special Publications*, 75(1), 195–203. <https://doi.org/10.1144/GSL.SP.1993.075.01.12>
- Rowland, J. C., Dietrich, W. E., & Stacey, M. T. (2010). Morphodynamics of subaqueous levee formation: Insights into river mouth morphologies arising from experiments. *Journal of Geophysical Research*, 115, F04007. <https://doi.org/10.1029/2010JF001684>
- Rowland, J. C., Stacey, M. T., & Dietrich, W. E. (2009). Turbulent characteristics of a shallow wall-bounded plane jet: Experimental implications for river mouth hydrodynamics. *Journal of Fluid Mechanics*, 627, 423. <https://doi.org/10.1017/S0022112009006107>
- Saito, Y., Wei, H., Zhou, Y., Nishimura, A., Sato, Y., & Yokota, S. (2000). Delta progradation and chenier formation in the Huanghe (Yellow River) delta, China. *Journal of Asian Earth Sciences*, 18(4), 489–497. [https://doi.org/10.1016/S1367-9120\(99\)00080-2](https://doi.org/10.1016/S1367-9120(99)00080-2)
- Saito, Y., Yang, Z., & Hori, K. (2001). The Huanghe (Yellow River) and Changjiang (Yangtze River) deltas: A review on their characteristics, evolution and sediment discharge during the Holocene. *Geomorphology*, 41(2-3), 219–231. [https://doi.org/10.1016/S0169-555X\(01\)00118-0](https://doi.org/10.1016/S0169-555X(01)00118-0)
- Sheets, B. A., Hickson, T. A., & Paola, C. (2002). Assembling the stratigraphic record: Depositional patterns and time-scales in an experimental alluvial basin. *Basin Research*, 14(3), 287–301. <https://doi.org/10.1046/j.1365-2117.2002.00185.x>
- Slingerland, R., & Smith, N. D. (2004). River avulsions and their deposits. *Annual Review of Earth and Planetary Sciences*, 32(1), 257–285. <https://doi.org/10.1146/annurev.earth.32.101802.120201>
- Smith, N. D., Cross, T. A., Dufficy, J. P., & Clough, S. R. (1989). Anatomy of an avulsion. *Sedimentology*, 36(1), 1–23. <https://doi.org/10.1111/j.1365-3091.1989.tb00817.x>
- Snyder, N. P., Wright, S. A., Alpers, C. N., Flint, L. E., Holmes, C. W., & Rubin, D. M. (2006). Reconstructing depositional processes and history from reservoir stratigraphy: Enlebright Lake, Yuba River, northern California. *Journal of Geophysical Research*, 111, F04003. <https://doi.org/10.1029/2005JF000451>
- Stouthamer, E., & Berendsen, H. J. A. (2001). Avulsion frequency, avulsion duration, and interavulsion period of Holocene channel belts in the Rhine-Meuse Delta, The Netherlands. *Journal of Sedimentary Research*, 71(4), 589–598. <https://doi.org/10.1306/112100710589>
- Sun, T., Paola, C., Parker, G., & Meakin, P. (2002). Fluvial fan deltas: Linking channel processes with large-scale morphodynamics. *Water Resources Research*, 38(8), 26–1–26–10. <https://doi.org/10.1029/2001WR000284>
- Swenson, J. B., Voller, V. R., Paola, C., Parker, G., & Marr, J. G. (2000). Fluvio-deltaic sedimentation: A generalized Stefan problem. *European Journal of Applied Mathematics*, 11, 433–452.
- Törnqvist, Torbjörn E. (1994). Middle and late Holocene avulsion history of the River Rhine (Rhine-Meuse delta, Netherlands). *Geology*, 22(8), 711. [https://doi.org/10.1130/0091-7613\(1994\)022h0711:MALHAH2.3.CO;2](https://doi.org/10.1130/0091-7613(1994)022h0711:MALHAH2.3.CO;2)
- van Gelder, A., van den Berg, J. H., Cheng, G., & Xue, C. (1994). Overbank and channelfill deposits of the modern Yellow River delta. *Sedimentary Geology*, 90(3–4), 293–305. [https://doi.org/10.1016/0037-0738\(94\)90044-2](https://doi.org/10.1016/0037-0738(94)90044-2)
- Wang, H., Bi, N., Saito, Y., Wang, Y., Sun, X., Zhang, J., & Yang, Z. (2010). Recent changes in sediment delivery by the Huanghe (Yellow River) to the sea: Causes and environmental implications in its estuary. *Journal of Hydrology*, 391(3–4), 302–313. <https://doi.org/10.1016/j.jhydrol.2010.07.030>
- Wang, S., Fu, B., Piao, S., Lü, Y., Ciais, P., Feng, X., & Wang, Y. (2015). Reduced sediment transport in the Yellow River due to anthropogenic changes. *Nature Geoscience*, 9, 38–41. <https://doi.org/10.1038/ngeo2602>
- Wang, Z.-Y., & Liang, Z.-Y. (2000). Dynamic characteristics of the Yellow River mouth. *Earth Surface Processes and Landforms*, 25(7), 765–782. [https://doi.org/10.1002/1096-9837\(200007\)25:7h765::AID-ESP98i3.0.CO;2-K](https://doi.org/10.1002/1096-9837(200007)25:7h765::AID-ESP98i3.0.CO;2-K)
- Wang, Y., Liu, X., Li, G., & Zhang, W. (2016). Stratigraphic variations in the Diaokou lobe area of the Yellow River delta, China: Implications for an evolutionary model of a delta lobe. *Geological Society, London, Special Publications*, 429(1), 185–195. <https://doi.org/10.1144/SP429.8>
- Wang, H., Yang, Z., Li, G., & Jiang, W. (2006). Wave climate modeling on the abandoned Huanghe (Yellow River) delta lobe and related deltaic erosion. *Journal of Coastal Research*, 224, 906–918. <https://doi.org/10.2112/03-0081.1>
- Wang, H., Yang, Z., Saito, Y., Liu, J. Paul, & Sun, X. (2006). Interannual and seasonal variation of the Huanghe (Yellow River) water discharge over the past 50 years: Connections to impacts from ENSO events and dams. *Global and Planetary Change*, 50(3–4), 212–225. <https://doi.org/10.1016/j.gloplacha.2006.01.005>
- Wang, H., Yang, Z., Saito, Y., Liu, J. Paul, Sun, X., & Wang, Y. (2007). Stepwise decreases of the Huanghe (Yellow River) sediment load (1950–2005): Impacts of climate change and human activities. *Global and Planetary Change*, 57(3–4), 331–354. <https://doi.org/10.1016/j.gloplacha.2007.01.003>
- Wells, N. A., & Dorr, J. A. (1987). Shifting of the Kosi River, northern India. *Geology*, 15(3), 204. [https://doi.org/10.1130/0091-7613\(1987\)15h204:SOTKRNI2.0.CO;2](https://doi.org/10.1130/0091-7613(1987)15h204:SOTKRNI2.0.CO;2)
- Whipple, K. X., Parker, G., Paola, C., & Mohrig, D. (1998). Channel dynamics, sediment transport, and the slope of alluvial fans: Experimental study. *The Journal of Geology*, 106(6), 677–694. <https://doi.org/10.1086/516053>
- Wolman, M. G., & Miller, J. P. (1960). Magnitude and frequency of forces in geomorphic processes. *The Journal of Geology*, 68(1), 54–74. <https://doi.org/10.1086/626637>
- Wu, X., Bi, N., Xu, J., Nitttrouer, J. A., Yang, Z., Saito, Y., & Wang, H. (2017). Stepwise morphological evolution of the active Yellow River (Huanghe) delta lobe (1976–2013): Dominant roles of riverine discharge and sediment grain size. *Geomorphology*, 292, 115–127. <https://doi.org/10.1016/j.geomorph.2017.04.042>
- Wu, X., Bi, N., Yuan, P., Li, S., & Wang, H. (2015). Sediment dispersal and accumulation off the present Huanghe (Yellow River) delta as impacted by the water-sediment regulation scheme. *Continental Shelf Research*, 111, 126–138. <https://doi.org/10.1016/j.csr.2015.11.003>
- Xu, J. (2003). Growth of the Yellow River delta over the past 800 years, as influenced by human activities. *Geografiska Annaler, Series A: Physical Geography*, 85(1), 21–30. <https://doi.org/10.1111/1468-0459.00186>
- Xue, C. (1993). Historical changes in the Yellow River delta, China. *Marine Geology*, 113(3–4), 321–330. [https://doi.org/10.1016/0025-3227\(93\)90025-Q](https://doi.org/10.1016/0025-3227(93)90025-Q)
- Yu, L. (2002). The Huanghe (Yellow) River: A review of its development, characteristics, and future management issues. *Continental Shelf Research*, 22(3), 389–403. [https://doi.org/10.1016/S0278-4343\(01\)00088-7](https://doi.org/10.1016/S0278-4343(01)00088-7)
- Yu, J., Fu, Y., Li, Y., Han, G., Wang, Y., Zhou, D., et al. (2011). Effects of water discharge and sediment load on evolution of modern Yellow River delta, China, over the period from 1976 to 2009. *Biogeosciences*, 8(9), 2427–2435. <https://doi.org/10.5194/bg-8-2427-2011>

- Yuill, B. T., Khadka, A. K., Pereira, J., Allison, M. A., & Meselhe, E. A. (2016). Morphodynamics of the erosional phase of crevasse-splay evolution and implications for river sediment diversion function. *Geomorphology*, 259, 12–29. <https://doi.org/10.1016/j.geomorph.2016.02.005>
- Zhang, X., Zhang, Y., Ji, Y., Zhang, Y., & Yang, Z. (2016). Shoreline change of the northern Yellow River (Huanghe) delta after the latest deltaic course shift in 1976 and its influence factors. *Journal of Coastal Research*, 74, 48–58. <https://doi.org/10.2112/SI74-005.1>
- Zheng, S., Edmonds, D. A., Wu, B., & Han, S. (2019). Backwater controls on the evolution and avulsion of the Qingshuigou channel on the Yellow River delta. *Geomorphology*, 333, 137–151. <https://doi.org/10.1016/j.geomorph.2019.02.032>
- Zheng, S., Wu, B., Wang, K., Tan, G., Han, S., & Thorne, C. R. (2017). Evolution of the Yellow River delta, China: Impacts of channel avulsion and progradation. *International Journal of Sediment Research*, 32, 34–44. <https://doi.org/10.1016/j.ijsrc.2016.10.001>
- Zhu, Y., Jia, X., & Shao, M. (2018). Loess thickness variations across the Loess Plateau of China. *Surveys in Geophysics*, 39(4), 715–727. <https://doi.org/10.1007/s10712-018-9462-6>